2019-06-01

Analytical Expressions for Acoustic Radiation Modes of Simple Curved Structures

Caleb Burley Goates
Brigham Young University

Analytical Expressions for Acoustic Radiation Modes of Simple Curved Structures

Caleb Burley Goates

A thesis submitted to the faculty of
Brigham Young University
in partial fulfillment of the requirements for the degree of

Master of Science

Scott D. Sommerfeldt, Chair
Jonathan D. Blotter
Kent L. Gee

Department of Physics and Astronomy

Brigham Young University

ABSTRACT

Analytical Expressions for Acoustic Radiation Modes
of Simple Curved Structures

Caleb Burley Goates
Department of Physics and Astronomy, BYU
Master of Science

The search for a convenient connection between vibration patterns on a structure and the sound radiated from that structure is ongoing in structural acoustics literature. Common techniques are wavenumber domain methods, or representation of the vibration in terms of some basis, such as structural modes or elementary radiators, and calculating the sound radiation in terms of the basis. Most choices for a basis in this situation exhibit strong coupling between the basis functions, but there is one choice which does not: Acoustic radiation modes are by definition the basis that orthogonalizes the radiation operator, meaning the radiation modes do not exhibit any coupling in radiation of sound.

Acoustic radiation modes are coming up on their 30th anniversary in the literature, but still have not found wide use. This is largely due to the fact that most radiation modes must be calculated through the computationally intensive boundary element method or boundary integral equations. Analytical expressions for radiation modes, or for the radiation resistance matrix from which they are derived, are only available for a few geometries. This thesis meets this problem head on, to develop additional analytical expressions for radiation resistance matrices of cylindrically curved structures.

Radiation modes are developed in the context of their use to calculate sound power. Experimental and computational sound power calculations are presented in order to validate the use of the modes developed here. In addition, the properties and trends of the developed modes are explored.

Keywords: acoustic radiation modes, sound power, structural acoustics

ACKNOWLEDGEMENTS

I would like to thank my current advisor and the many mentors I have had during my time at Brigham Young University. They have all contributed significantly to the person and scholar that I am. Dr. Scott Sommerfeldt, for teaching me how to see all sides of a question and for encouraging me to pursue magematical approaches to problems; Dr. Traci Neilsen for helping me see my potential, teaching me how to write academically, and being the teacher I have taken the most classes from; Dr. Kent Gee for his writing tips and friendship, and for being my side advisor throughout my undergraduate and graduate degrees; and Dr. Jon Blotter for his enthusiasm, encouragement, and confidence in me.

Thanks are due to Cameron Jones, who worked with me on much of this project and forged the trail before me so I could avoid certain pitfalls. Also, thanks to Michael Rose and Nathaniel Wells, my office mates, for allowing me to bounce questions off them.

Finally, I would like to thank my family, my wife and two boys. I know it has not been easy for them to get me through this degree, but I could not have done it without their support.

TABLE OF CONTENTS

LIST OF FIGURES

LIST OF TABLES

Chapter 1

Introduction

This thesis details work toward developing a precision-grade sound power estimation method based on vibration measurements. This method consists of taking measurements of a vibrating structure using a scanning laser Doppler vibrometer, then processing the resulting data with acoustic radiation modes to calculate the sound power. The specific contribution of this thesis is the development and testing of several new acoustic radiation mode formulations.

1.1 Background

Sound power is simply the total power radiated by an object in the form of sound. In contrast to pressure and other acoustic measurements, sound power does not depend on the distance from the source but is simply a property of the source itself. As such, it is a good quantifier of the overall noise safety of an object.

Because sound power includes all the sound output by a source, measurements to estimate it are usually very involved and cumbersome. Existing estimation methods which have been standardized by the International Organization for Standardization (ISO) include pressure-based

methods and intensity-based methods. Some of these use known acoustic environments, e.g., reverberation chambers, and the others often involve pressure measurements over a surface that encloses that source, which require elaborate path traversals or many microphones. In addition, the up-front cost involved in installing a specialized acoustic testing room such as an anechoic or reverberation chamber can be prohibitive. The two ISO standardized vibration-based methods are only qualified to give engineering and survey grade results.

Theory for a radiation mode and vibration based sound power estimation method has been present in the literature since the early 1990s, when radiation modes were first introduced, though experimental verification of it has largely been untouched. In June 1990, Borgiotti published a paper with the title "The power radiated by a vibrating body in an acoustic fluid and its determination from boundary measurements,"[1] in which he showed it possible analytically to calculate sound power from known vibration. Several other papers have built on his method and used it numerically,[2] but experimental validation of the method was not published until twelve years later, when Bai gave calculations of the sound power of a baffled flat plate measured with a laser displacement sensor.[3] Since then there have been no other experimental validations published, to the knowledge of the author. Other methods have also been proposed for calculating sound power from known surface vibrations,[4] but these, too, have been mainly focused on numerical scenarios, and have not been developed into an experimental method for estimating sound power from vibration measurements.

The theory of radiation modes can be derived from standard expressions for sound power. Sound power in the frequency domain may be expressed in terms of the acoustic pressure, $\tilde{p}$, and the acoustic particle velocity, $\vec{\tilde{v}}$, as

$$\Pi = \frac{1}{2}\int_S \mathrm{Re}\{\tilde{p}^* \vec{\tilde{v}} \cdot \vec{n}\}\, dS, \tag{1-1}$$

where $(\cdot)^*$ denotes complex conjugate, S is a surface that encloses the sound source, and $\vec{n}$ is the outward facing normal to that surface. If the surface S is allowed to coincide with the vibrating surface of the source itself, then the particle velocity may be replaced with the normal surface velocity $\tilde{u}$ as

$$\Pi = \frac{1}{2}\int_S \mathrm{Re}\{\tilde{p}^* \tilde{u}\}\, dS. \tag{1-2}$$

One method of performing this integration is to discretize the vibrating surface into N small elements with area $S_e = S/N$ and assume that the pressure and normal surface velocity are constant over each element. The integral then becomes a summation, which can be written in vector form as

$$\Pi = \frac{S_e}{2}\mathrm{Re}\{\boldsymbol{p}^H \boldsymbol{u}\}, \tag{1-3}$$

where $\boldsymbol{p}$ and $\boldsymbol{u}$ are $1 \times N$ vectors containing the pressure and normal surface velocity, respectively, of each discrete element on the structure, and $(\cdot)^H$ denotes the Hermitian transpose. This expression can be further simplified to remove the need for measured pressures using the matrix of self and mutual impedances of the discrete elements. This matrix, $\mathbf{Z}$, is populated with Green's functions between each elemental location on the vibrating structure, and allows the pressure to be written in terms of the velocities, as

$$\boldsymbol{p} = \mathbf{Z}\boldsymbol{u}\,. \tag{1-4}$$

Equation (1-3) then further simplifies to

$$\Pi = \frac{S_e}{2}\mathrm{Re}\{\boldsymbol{u}^H\mathbf{Z}\boldsymbol{u}\} = \frac{S_e}{2}\boldsymbol{u}^H\mathrm{Re}\{\mathbf{Z}\}\boldsymbol{u} \tag{1-5}$$

where the equalities rely on the fact that $\boldsymbol{Z}$ is Hermitian. Finally, the radiation resistance matrix is often introduced to further simplify this expression:

$$\mathbf{R} = \frac{S_e}{2}\mathrm{Re}\{\mathbf{Z}\}, \tag{1-6}$$

and therefore

$$\Pi = \boldsymbol{u}^H\mathbf{R}\boldsymbol{u}\,. \tag{1-7}$$

The acoustic radiation modes $\boldsymbol{q}_r$ are the eigenvectors of **R**, with the eigenvalues λ_r being related to the efficiencies of the corresponding radiation modes. These modes provide a convenient way to analyze a given **R**, and they may also be used to calculate sound power as

$$\Pi = \sum_{r=1}^{N} \lambda_r |\tilde{y}_r|^2 \tag{1-8}$$

where $\tilde{y}_r = \boldsymbol{q}_r \cdot \boldsymbol{u}$.

It is important to note that the acoustic radiation modes are not the structural modes commonly used to describe the vibration of a structure. While the structural modes depend on the material, mounting conditions, and internal geometry of the structure, acoustic radiation modes are independent of these and depend only upon the geometry of the structure-fluid interface. The first few radiation modes and structural modes are shown in Fig. 1-1 for a rectangular simply-supported plate at a very low frequency. While the structural modes all go to zero at the edges of the plate to satisfy the simply supported condition, the radiation modes do not.

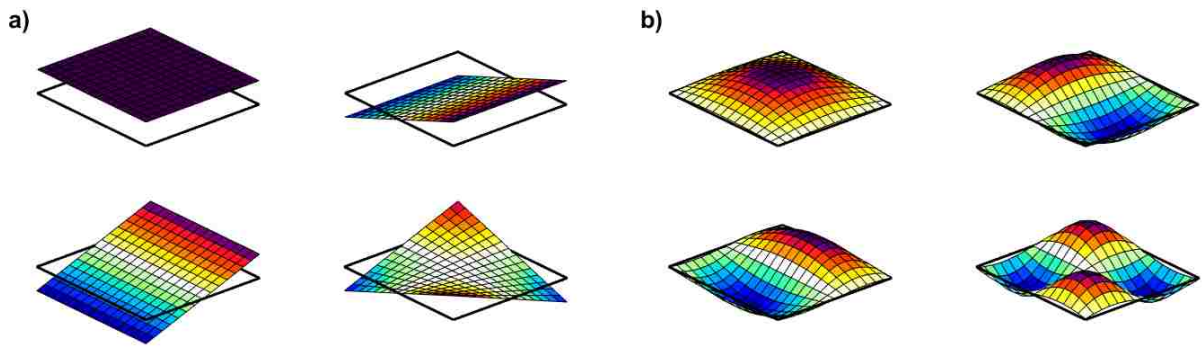

Figure 1-1: A comparison of the first four radiation modes and structural modes for a simply supported plate. (a) The first four radiation modes of a baffled flat plate. (b) The first four structural modes of a simply supported plate.

Expressions for **R** and $\boldsymbol{q}_r$ are known for some simple geometries, but must be calculated for other geometries using boundary integral equations or the boundary element method. The ijth element of **R** for a flat plate is[5]

$$\mathrm{R}_{ij} = \frac{\rho_0 \omega^2 S_e^2}{4\pi c} \frac{\sin k d_{ij}}{k d_{ij}}, \tag{1-9}$$

where ρ_0 and c are the density and sound speed of the acoustic fluid, ω is the angular frequency, k is the acoustic wavenumber, and d_{ij} is the distance between the ith and jth elements. In addition, the $\boldsymbol{q}_r$ of spherical geometries are known to be the spherical harmonics.[6] The evaluation of these is much more computationally efficient than a boundary integral formulation that is commonly required for other geometries. Hence, this work develops and presents other analytical or quasi-analytical formulations for **R** of various geometries. Specifically, this work will focus on cylindrically curved structures and variations thereupon.

1.2 Thesis Overview

The thesis is outlined as follows: Following this introductory first chapter, Chapter 2 presents a theoretical and experimental treatment of sound power radiation from vibrating

cylinders. Chapter 3 investigates the trends and properties of the cylinder radiation modes in more detail, including generalization of the modes to partial cylinders. Chapter 4 then discusses the use of these modes on slightly curved plates, and includes an additional radiation mode formulation specific to that scenario. Finally, Chapter 5 summarizes the findings of the previous three chapters, drawing conclusions as appropriate. Chapter 2 was a joint effort with Cameron Jones, who also included those results in his thesis. His work focused on the computational and experimental realizations of the radiation mode method, while my work in that chapter included the development of the radiation modes and the boundary element method verifications.

Chapter 2

Sound Power of Vibrating Cylinders

2.1 Introduction

Many methods exist for measuring sound power. The International Organization for Standardization (ISO) has published ten standards and two technical specifications detailing how to obtain sound power measurements. None of the standardized methods are based on vibration measurements, and the two technical specifications give only engineering or survey grade results; there is no precision grade vibration-based method. In the early 1990s, theory was developed for a method which could potentially fill this void; this method calculates sound power based on a combination of measured surface vibrations of a structure and acoustic radiation modes.[5]

Acoustic radiation modes provide a convenient basis with which to describe sound radiation from a structure. Structural vibration modes describe the displacement of a structure and satisfy the structural equations of motion and boundary conditions. Conversely, acoustic radiation modes describe the acoustic field; these modes are orthogonal with respect to sound radiation and

allow the surrounding acoustical field to be calculated based on the vibrations of a structure. Acoustic radiation modes can be derived from the radiation resistance matrix. The radiation resistance matrix **R** relates the normal surface velocities from discrete elements of the structure to the radiated sound power of the structure through the equation

$$\Pi(\omega) = \boldsymbol{u}^{\mathrm{H}}(\omega)\mathbf{R}(\omega)\boldsymbol{u}(\omega), \tag{2-1}$$

where $\boldsymbol{u}$ is a column vector containing the normal velocity at each discrete element, $(\cdot)^H$ signifies the Hermitian transpose, and ω is the frequency of interest.[7] The dependence of various quantities on ω is implied in expressions throughout the remainder of this paper and will be omitted. The eigenvectors of the radiation resistance matrix are the acoustic radiation modes, and the corresponding eigenvalues are proportional to the radiation efficiencies of the eigenvectors. The sound power can be written in terms of the acoustic radiation modes $\boldsymbol{q}_r$ and eigenvalues λ_r as

$$\Pi = \sum_{r=1}^{N} \lambda_r |\tilde{y}_r|^2 \tag{2-2}$$

where $\tilde{y}_r = \boldsymbol{q_r} \cdot \boldsymbol{u}$, and N is the number of elementary radiators over the surface of the structure.[7]

Though the theory behind this approach to calculating sound power has been present for decades, experimental validations did not come until more recently. In 2002, Bai et al. published the first experimental sound power calculations based on acoustic radiation modes.[3] Their work showed sound power calculations on baffled flat plates using the most efficiently radiating modes at low frequencies and a modified approach at higher frequencies. The paper showed good agreement between Bai's method and standardized sound power measurements at low frequencies, but the results diverged at higher frequencies. More recent research has shown that acoustic radiation modes can be used to calculate the individual contributions to sound power from multiple uncorrelated sources in a system without having to isolate the sources individually.[8] This research

used the vibration-based radiation mode (VBRM) method, which will be used throughout this thesis. The VBRM method consists of using complex surface velocity measurements with the radiation resistance matrix to compute the sound power.

In addition to sound power calculations, radiation modes have found use in the field of Active Structural Acoustic Control (ASAC).[5,9,10] They have been used for power calculations in computational experiments since they were first introduced. For example, numerical simulations on effectiveness of ASAC control parameters has relied on the radiation modes for evaluation of sound power.[11] Radiation modes have also been used as a guide for structural design, where certain efficient radiation vibration patterns are suppressed through structural modifications.[12] Recent work shows that radiation modes may be used as a basis set for acoustical holography source reconstruction.[13]

Many of the early papers on radiation modes present results for cylinders. The three papers that introduced radiation modes included a finite cylinder with hemispherical endcaps[6] and two finite cylinders with flat endcaps.[1,14] In each of these cases, only the axisymmetric modes were calculated. These modes were found by an unspecified numerical method, boundary integral methods, and the boundary element method (BEM), respectively. In addition, at least one other paper has treated the hemispherically capped finite cylinder.[15] Through all these publications there has never been a full development of the radiation modes for a cylinder such that the sound power could be calculated. Boundary element methods or boundary integral equations can be used to calculate the radiation resistance matrix,[13] but an analytical formulation is desirable, as it has the potential to reduce complexity and computational load. More recently, Aslani et al.[16] published a formulation for radiation modes of a finite cylinder sandwiched between two infinite pressure release planes using eigenfunction expansion. This paper will closely follow the formulation of

Aslani et al. to develop a full analytical expression for the radiation resistance matrix of vibrating cylinders with infinite cylindrical baffles. These cylindrical radiation modes will provide an additional resource, allowing for the calculation of sound power of cylindrical objects.

2.2 Cylinder Radiation Modes

2.2.1 Eigenfunction formulation of the radiation resistance matrix

The radiation resistance matrix is derived from the pressure that a small vibrating element of a structure generates across the structure. Assume that a small portion of a hard, infinite cylinder is vibrating with velocity

$$u(\theta, z) = \begin{cases} u_0 & \theta_1 \le \theta \le \theta_2, z_1 \le z \le z_2 \\ 0 & \text{otherwise} \end{cases} \tag{2-3}$$

for some θ_1, θ_2 and z_1, z_2 such that $a\Delta\theta \equiv a(\theta_2 - \theta_1) \ll 2\pi/k$ and $\Delta z \equiv (z_2 - z_1) \ll 2\pi/k$, where k is the acoustic wavenumber and a is the radius of the cylinder. This vibration creates a pressure field that can be written in terms of cylindrical eigenfunctions as

$$\begin{aligned} p(r, \theta, z) = \sum_{m=0}^{\infty} \int_0^{\infty} dk_z \, (A_m \cos m\theta + B_m \sin m\theta) \\ \times (D(k_z) \cos k_z z + E(k_z) \sin k_z z) H_m^{(2)}(k_r r), \end{aligned} \tag{2-4}$$

where $k_r = \sqrt{k^2 - k_z^2}$, k_z is the axial acoustic wavenumber, m is an integer, $H_m^{(2)}(x)$ is the mth-order Hankel function of the second kind, and A_m, B_m, $D(k_z)$, and $E(k_z)$ are coefficients yet to be determined. The Hankel function of the first kind is omitted as the absence of sources outside $r = a$ precludes incoming cylindrical waves. The coefficients are determined by the surface condition at $r = a$ of

$$\left.\frac{\partial p}{\partial r}\right|_{r=a} = -j\rho_0\omega\, u(\theta, z), \tag{2-5}$$

where ρ_0 is the density of air, ω is the angular frequency, and $j = \sqrt{-1}$. To apply this boundary condition, the velocity is expanded in terms of the θ and z cylindrical eigenfunctions as

$$u(\theta, z) = \int_0^\infty dk_z\, (d(k_z)\cos k_z z + e(k_z)\sin k_z z) \sum_{m=0}^{\infty} (a_m \cos m\theta + b_m \sin m\theta). \tag{2-6}$$

Equation (2-6) can be set equal to Eq. (2-3) to find the coefficients a_m, b_m, $d(k_z)$ and $e(k_z)$. Because Eq. (2-6) is a separable expression, the θ and z dependence may be treated separately:

$$\sum_{m=0}^{\infty} (a_m \cos m\theta + b_m \sin m\theta) = \begin{cases} u_0 & \theta_1 \le \theta \le \theta_2 \\ 0 & \text{otherwise} \end{cases}, \tag{2-6a}$$

$$\int_0^\infty (d(k_z)\cos k_z z + e(k_z)\sin k_z z) dk_z = \begin{cases} 1 & z_1 \le z \le z_2 \\ 0 & \text{otherwise} \end{cases}, \tag{2-6b}$$

where the constant u_0 has been arbitrarily assigned to the θ-dependent expression. The coefficients may now be solved for using orthogonality and sine and cosine transforms:

$$\begin{aligned} a_m &= \frac{u_0}{\pi}\int_{\theta_1}^{\theta_2} \cos m\theta\, d\theta \approx \frac{u_0 \Delta\theta}{\pi}\cos m\theta_0, \\ b_m &= \frac{u_0}{\pi}\int_{\theta_1}^{\theta_2} \sin m\theta\, d\theta \approx \frac{u_0 \Delta\theta}{\pi}\sin m\theta_0, \\ d(k_z) &= \frac{1}{\pi}\int_{z_1}^{z_2} \cos k_z z\, dz \approx \frac{\Delta z}{\pi}\cos k_z z_0, \\ e(k_z) &= \frac{1}{\pi}\int_{z_1}^{z_2} \sin k_z z\, dz \approx \frac{\Delta z}{\pi}\sin k_z z_0, \end{aligned} \tag{2-7}$$

where $z_0 = (z_2 + z_1)/2,\ \Delta z = z_2 - z_1,\ \theta_0 = (\theta_2 + \theta_1)/2,\ \Delta\theta = \theta_2 - \theta_1$. The approximate equalities hold because Δz and $a\Delta\theta$ are small compared to a wavelength. Substituting Eq. (2-7) into Eq. (2-6), applying the boundary conditions in Eq. (2-5), and simplifying results in the final pressure expression,

$$p(r,\theta,z) = -j\frac{u_0\rho_0\omega\Delta\theta\Delta z}{\pi^2}\int_0^\infty \frac{dk_z}{k_r}\cos[k_z(z-z_0)]\sum_{m=0}^{\infty}\frac{H_m^{(2)}(k_r r)}{H_m^{(2)'}(k_r a)}\cos[m(\theta-\theta_0)]. \quad (2\text{-}8)$$

Dividing Eq. (2-8) by the velocity of the vibrating element, i.e., u_0, and evaluating at a surface point gives the mutual impedance between the source point, point i, and the field point, point j such that

$$Z_{ij} = -j\frac{\rho_0\omega\Delta\theta\Delta z}{\pi^2}\int_0^\infty \frac{dk_z}{k_r}\cos\left[k_z(z_j-z_i)\right]\sum_{m=0}^{\infty}\frac{H_m^{(2)}(k_r a)}{H_m^{(2)'}(k_r a)}\cos\left[m(\theta_j-\theta_i)\right]. \quad (2\text{-}9)$$

The radiation resistance matrix is concerned only with the real part of this expression. Thus, since $H_m^{(2)}(k_r a)/k_r H_m^{(2)'}(k_r a)$ is purely real for imaginary k_r, the integration need only be carried out from 0 to k. The elements of the radiation resistance matrix are then found as

$$\begin{aligned} R_{ij} &= \frac{S_e}{2}\mathrm{Re}\{Z_{ij}\} \\ &= \frac{S_e^2\omega\rho_0}{a\pi^2}\int_0^k \frac{dk_z}{k_r}\cos\left[k_z(z_j-z_i)\right]\sum_{m=0}^{\infty}\mathrm{Im}\left\{\frac{H_m^{(2)}(k_r a)}{H_m^{(2)'}(k_r a)}\right\}\cos\left[m(\theta_j-\theta_i)\right], \end{aligned} \quad (2\text{-}10)$$

where $S_e = a\Delta\theta\Delta z$ is the area of a single discrete element of the structure, and the summation has been moved inside the integral.

2.2.2 Numerical evaluation

Equation (2-10) is not closed-form; it involves an infinite sum that must be truncated and an integral that must be numerically evaluated. This section offers guidance on how the expression may be evaluated.

The sum is performed first for each integration point. As m increases the ratio $\mathrm{Im}\left\{H_m^{(2)}(k_r a)/H_m^{(2)'}(k_r a)\right\}$ decreases, approaching zero rapidly after $m \approx k_r a$. Therefore, this coefficient is used as the test for convergence. For the purposes of this research, once $\mathrm{Im}\left\{H_m^{(2)}(k_r a)/H_m^{(2)'}(k_r a)\right\} < 10^{-8}$, the sum is considered to have converged.

The truncated sums may be calculated at desired integration points as dictated by a given integration method. This paper uses the midpoint rule, with the integrand evaluated at 80 points over the interval $[0, k]$. Though this is a rather simple method to perform the integration, it has been shown to be sufficiently accurate for the purposes of this research.

It appears there could be a singularity in the integral at $k_z = k$, where k_r becomes zero. Use of the limiting forms of the Hankel functions as the argument goes to zero shows that $\lim_{k_r \to 0} \mathrm{Im}\left\{H_m^{(2)}(k_r a)/H_m^{(2)'}(k_r a)\right\}/k_r = 0$, so the integrand may be replaced with zero at the endpoint if it is needed for the chosen integration method.

2.2.3 Radiation modes

Acoustic radiation modes are computed with an eigendecomposition of the radiation resistance matrix[14] and provide a useful way to characterize **R**. The eigenvectors represent the acoustic radiation modes while the associated eigenvalues are proportional to the radiation efficiency. The first nine radiation modes from the formulation above, ordered by the radiation efficiency of the mode, are shown in Fig. 2-1 for a cylinder with $a/L = 0.2$ at $ka = 0.01$ rad. The

first mode resembles a monopole with all parts of the cylinder vibrating in phase and at equal amplitude. The next three modes resemble dipoles and the final five modes resemble quadrupoles. Due to the symmetries associated with a cylinder, all radiation modes with θ dependence come in pairs of degenerate modes.

Figure 2-2 shows the nine most efficient radiation modes for $ka = 1$. The first four modes follow the same pattern exhibited in Fig. 2-1, though the amplitude is tapered toward the ends of the cylinder. The fifth mode in Fig. 2-2 is the seventh mode from Fig. 2-1, which has overtaken the fifth and sixth modes from Fig. 2-1 in radiation efficiency. The eighth and ninth modes in Fig. 2-2 are new modes which were not seen in Fig. 2-1.

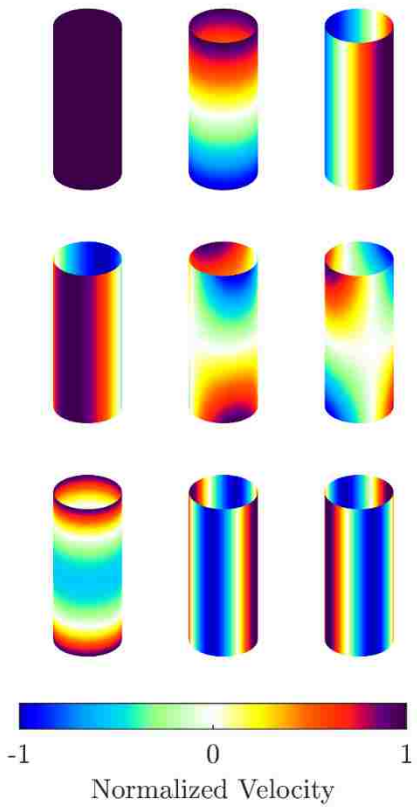

Figure 2-1: The nine most efficient radiation modes for a baffled cylinder with a/L=0.2 **and** ka=0.01**.**

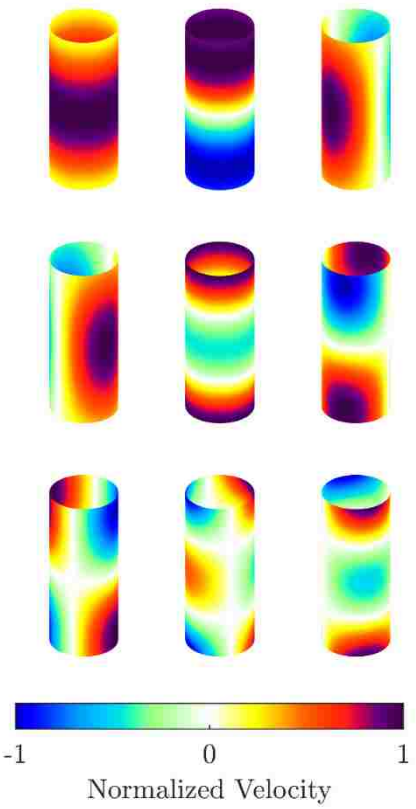

Figure 2-2: The nine most efficient radiation modes for a baffled cylinder with a/L=0.2 **and** ka=1**.**

The modal efficiencies with respect to ka also give insight into the modal behavior. Efficiencies are plotted in Fig. 2-3 for each of the nine modes shown in Fig. 2-1, with degenerate mode efficiencies combined into one line. This plot shows the monopole/dipole/quadrupole radiation characteristics of the modes at low ka: The first mode increases in efficiency, and therefore power, at a rate of 6 dB/octave, the next three modes at 12 dB/octave, and the last five at 18 dB/octave.

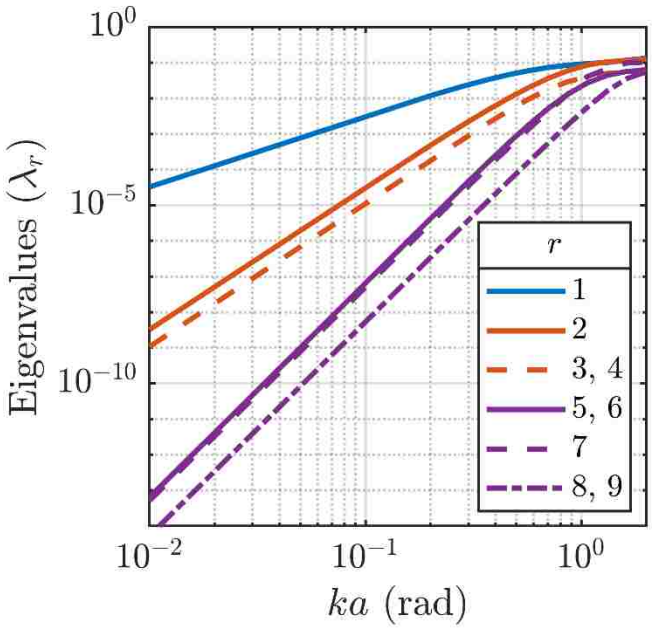

Figure 2-3: Efficiencies of the nine radiation modes that are most efficient at low ka. Degenerate mode efficiencies are combined into one line.

Sound power can be calculated using either the radiation resistance matrix as in Eq. (2-1), or the acoustic radiation modes, as in Eq. (2-2). Use of the radiation resistance matrix requires a matrix-vector multiplication and a dot product while use of acoustic radiation modes requires an eigenvalue decomposition of a matrix, several dot products to find $\tilde{y}_r$, and a sum. Since the complexity of eigenvalue decomposition is theoretically limited to that of matrix-vector multiplication[17,18] and is in practice much slower, there is no benefit to using the acoustic radiation

modes for the sound power calculation presented in this work. It is possible that interpolation of the radiation modes could, in some future work, make radiation modes faster for power computation, but in the simple uses described by Eqs. (2-1) and (2-2) there is no real benefit to using the radiation modes. The VBRM power curves in this paper are therefore calculated using the radiation resistance matrix as demonstrated in Eq. (2-1). For brevity, the cylindrical radiation resistance matrix will not be explicitly mentioned in the following sections, however when the VBRM method is used in this paper it is with the radiation resistance matrix given in Eq. (2-10), and the following validations treat both the method and the resistance matrix.

2.3 Computational Verification of Sound Power Calculations

To verify the methodology above, sound power calculations performed using the VBRM method as just described were compared to those performed with the boundary element method (BEM). BEM simulations were performed using VibroAcoustics One (VA One), a commercial package produced by the ESI Group. The comparison was conducted on a 41 cm cylinder with a 7.6 cm radius. The infinite cylindrical baffle assumed in the theory was approximated in these simulations by a 1-meter baffle connected to each end of the vibrating portion of the cylinder. Simulations were also performed with rigid ends on the cylinder instead of a baffle, and these results showed that the baffle had a negligible effect on the radiated sound power.

Once the cylinder was modeled in VA One, the surface velocities of the shell were computed at each nodal point of the cylindrical mesh using the modal expansion method developed by Bernoulli for a cylinder excited by a point force.[18] For each location on the mesh created in VA One, the complex surface velocities were calculated using

$$u_3(x,\theta) = \frac{2P}{\rho haL\pi} \sum_{m=1}^{\infty} \sum_{n=0}^{\infty} \frac{\sin(m\pi z^*/L)\sin(m\pi z/L)\cos n(\theta-\theta^*)}{\varepsilon_n \omega_{mn}^2 \sqrt{[1-(\omega/\omega_{mn})^2]^2 + 4\zeta_{mn}^2(\omega/\omega_{mn})^2}} e^{-j\phi_{mn}} \qquad (2\text{-}11)$$

where P is the point load, ρ is the density of the cylinder's material, h is the thickness of the cylindrical wall, L is the length of the cylinder, m and n are the longitudinal and radial mode numbers, respectively, z^* and θ^* are the longitudinal and radial location of the point force, z and θ are the longitudinal and radial locations of the nodal points, ω is the angular frequency of interest, ω_{mn} is the natural angular frequency of a given mode, ζ is a damping coefficient,

$$\phi_{mn} = \tan^{-1} \frac{2\zeta_{mn}(\omega/\omega_{mn})}{1-(\omega/\omega_{mn})^2}, \qquad (2\text{-}12)$$

and

$$\varepsilon_n = \begin{cases} 1 & n \neq 0 \\ 2 & n = 0 \end{cases}. \qquad (2\text{-}13)$$

These velocities were supplied to the VA One BEM simulation, which was then used to calculate the sound power of the cylinder. Equation (2-11) was also used to calculate the surface velocities used as inputs into the VBRM method.

Multiple simulations were run in VBRM using different spatial sampling grids and different numbers of points to analyze the effect of the spatial sampling. Velocities were calculated with the following spatial sampling patterns (longitudinal points x theta points): 8x9 (72 points), 10x12 (120 points), 16x19 (304 points) and 26x31 (804 points). Figure 2-4 shows the computational results using the VBRM method for each of these grids. The 72-point spatial sampling simulation agrees with simulations using a denser spatial sample below 1.5 kHz. Above 1.5 kHz the results begin to diverge. The 120-point spatial sampling simulation agrees with simulations using a denser spatial sample until 3 kHz, after which the results diverge. The reason

for the divergence of the 72- and 120-point simulations is due to the low spatial sampling density associated with fewer data points. The 304-point simulation and the 806-point simulation agree exactly throughout the 6 kHz range shown on the plot.

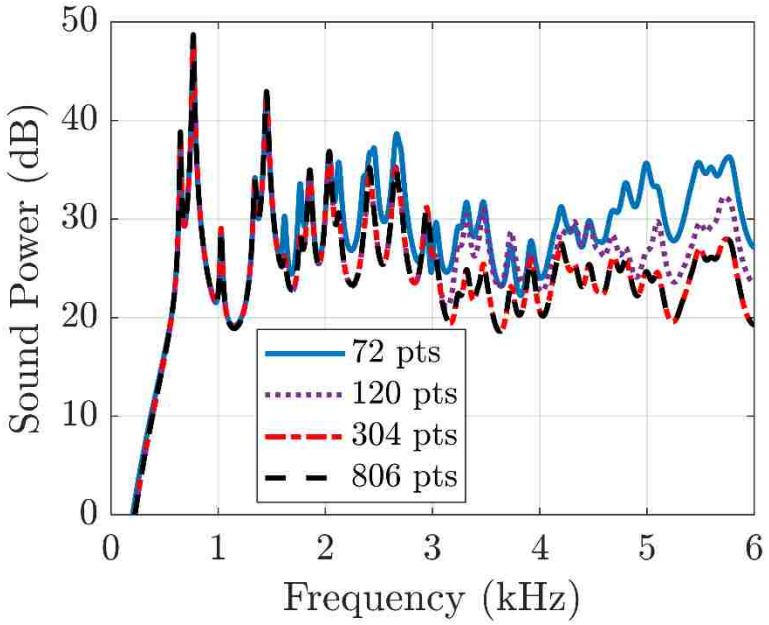

Figure 2-4: Numerically calculated sound power using the radiation resistance matrix and simulated complex velocities at several different numbers of data points.

The sound power results from the 304-point simulation shown in Fig. 2-4 were compared with the sound power results calculated using the BEM method. These results are shown in Fig. 2-5, with the two methods giving nearly identical results at most frequencies. The VBRM method calculates sound power to be slightly higher between 1.5 kHz and 2 kHz and again between 3 kHz and 4 kHz but the difference between the two methods is less than 1.5 dB at almost all frequencies.

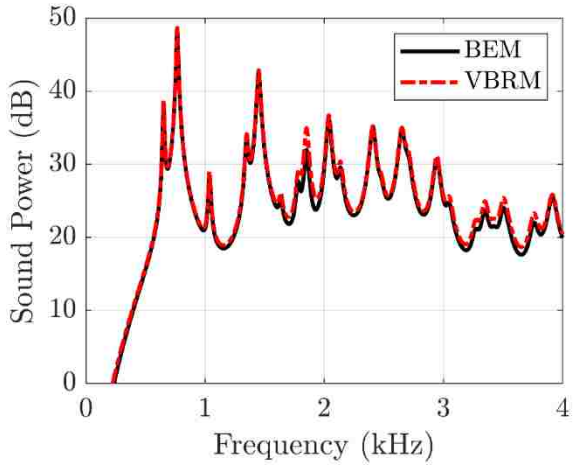

Figure 2-5: Numerically derived sound power of a 41 cm long cylinder with a 7.6 cm radius using the VBRM and BEM methods.

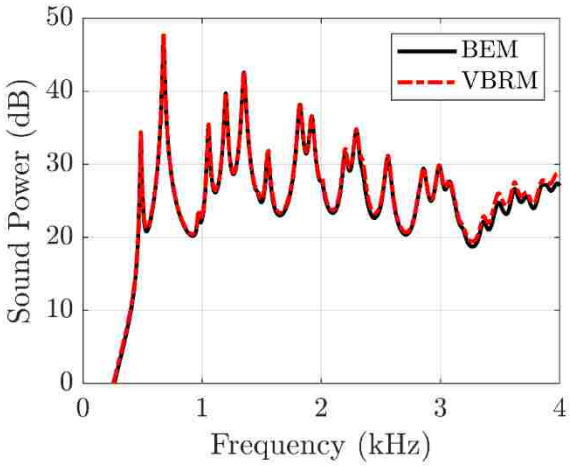

Figure 2-6: Numerically derived sound power of a 41 cm long cylinder with a 15.2 cm radius using the VBRM and BEM methods.

The VBRM method and BEM method were also used to calculate the sound power of a 41 cm long cylinder with a 15.2 cm radius. Due to the larger surface area of the 15.2 cm radius cylinder, the number of points used in the VBRM simulation was increased to 576 to ensure the spatial sampling was dense enough for accurate results. Figure 2-6 shows the comparison between the two methods for this cylinder. Like the results from the 7.6 cm radius cylinder, the results from the two methods for the 15.2 cm radius cylinder line up at most frequencies, with slight discrepancies at frequencies higher than 3 kHz. These discrepancies are less than 1.5 dB.

2.4 Experimental Verification of Sound Power Calculations

This section will detail the experimental sound power measurement of a cylinder using the VBRM method. The results calculated using the VBRM method will then be compared to sound power measurements taken using ISO 3741 in a large reverberation chamber, with the results being reported in one-third octave bands.

2.4.1 Experimental setup and measurement of a cylindrical shell

A 41 cm long aluminum cylinder with a radius of 7.6 cm and flat endcaps was mounted on a plywood board. A Modal Shop 2007E shaker was supported by the same plywood board with a small piece of foam minimizing the transfer of vibrations from the shaker to the plywood. The stinger of the shaker was attached to the cylinder 8.5 cm from its bottom edge. The mounted cylinder and shaker were then attached to an Outline ET250-3D electronic turntable and placed in a reverberation chamber with approximate dimensions 5m x 6m x 7m (see Fig. 2-7). In preparation to make ISO 3741 sound power measurements, six microphones were set up inside the reverberation chamber according to guidelines of the standard.

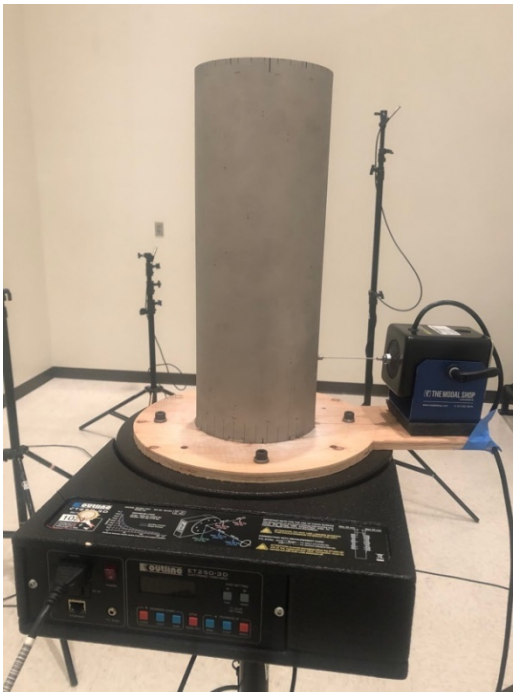

Figure 2-7: Setup of a mounted cylinder on a turntable with a shaker to excite the cylinder. The microphones and reverberation chamber used for ISO 3741 are seen in the background.

It is important to note the experimental setup described above does not perfectly match the theoretical and computational assumptions presented in previous sections. Previous sections

assumed an infinite cylindrical baffle (approximated by a 1-meter baffle in VA One) extending from the end of each cylinder, and simulations treated a simply-supported cylinder. While acoustic radiation modes are independent of structural boundary conditions, the lack of a cylindrical baffle and the inclusion of a turntable and wooden base are departures from previously made assumptions. The case of a cylinder without a baffle was also tested using BEM, and the baffle changed the results by less than 0.3 dB at any given frequency, so those departures are not expected to significantly alter the results.

The shaker was excited using pseudo-random noise between 0 and 12.4 kHz. Using a scanning laser Doppler vibrometer (SLDV), line scans measuring the complex surface velocities of the cylinder were taken at 10-degree intervals around the circumference of the cylinder. Each line scan contained 31-points, resulting in a total of 1,116 scan points over the surface of the cylinder. This number of experimental points was well above the number of points needed to obtain accurate results up to 6 kHz, as shown in Fig. 2-4. Figure 2-8 shows an example of one line scan.

Figure 2-8: Example of one of the 36 line scans taken over the surface of the cylinder to measure complex surface velocities.

A small section of the cylinder was blocked by the shaker so that surface velocity measurements using the SLDV were unattainable. Velocity data from surrounding points were used to approximate the velocity data of these blocked points. There were a total of 25 out of the 1,116 scan points where the velocity data was approximated using surrounding points. It is notable that due to the proximity of the blocked portions of the cylinder to the point of excitation on the cylinder, the approximated velocity data at those points is expected to be underestimated. The resulting velocity data collected by the SLDV were then used as inputs to the VBRM method.

After the surface velocity measurements were collected, the SLDV was removed from the reverberation chamber, and sound pressure measurements were taken according to the procedures set forth in ISO 3741. Sound power was calculated according to ISO 3741, and the calculated sound power measurements using the VBRM method were then compared to these standard results, which are reported in one-third octave bands.

2.4.2 Sound power results of the cylinder

Figure 2-9 shows the comparison between the VBRM method and the ISO 3741 sound power results. The results are also summarized in Table I which shows the difference between the methods at each one-third octave band. Below 200 Hz the ISO measured sound power results were within 10 dB of the noise floor of the chamber. Therefore, the results should be considered upper bounds of the radiated sound power at these frequencies. Between the 200 Hz and 10 kHz one-third octave bands there is good alignment between the two methods. In this region the mean difference between the two methods was 0.1 dB with a standard deviation of 1.4 dB. The maximum one-third octave band difference was 2.5 dB at the 400 Hz band. These experimental differences are in line with the differences seen between the BEM and VBRM methods compared in Figs. 2-

5 and 2-6. In addition, the overall levels are extremely close, as seen in Table 2-1, with only 0.4 dB difference between the two methods.

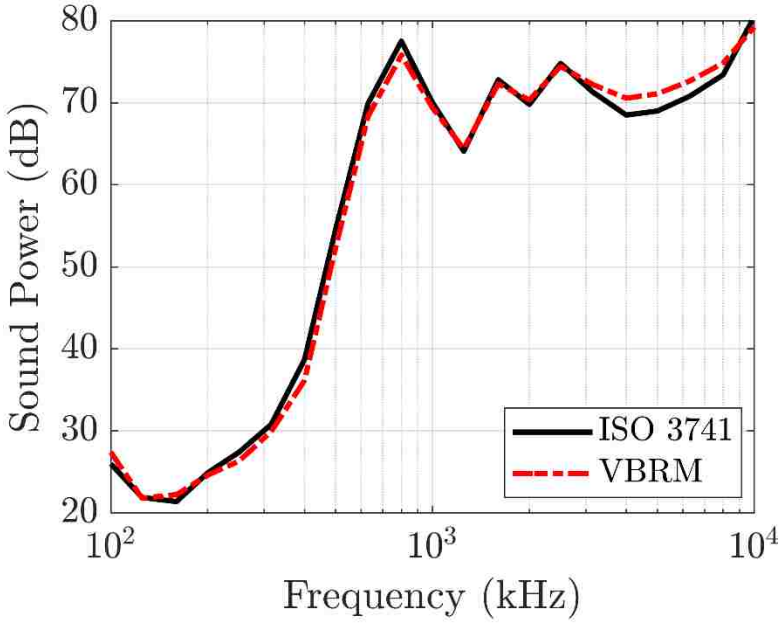

Figure 2-9: Results of the sound power measurements using the VBRM method compared to the ISO 3741 standard results.

The differences between the two methods could also be the result of the experimental setup. The theoretical and computational work assumed an infinitely baffled cylinder, but the experimental setup included endcaps on each end of the cylinder instead of a baffle. The endcaps could have radiated noise contributing to the sound power measured by ISO 3741. The experimental setup of the cylinder also included a plywood mount, a turntable, and a shaker, each of which could have vibrated from contact with cylinder. These surfaces were not measured using the SLDV, thus any contribution they made to sound power would be measured by ISO 3741 but not by the VBRM method.

Table 2-1: Results of the sound power measurements using ISO 3741 and the VBRM method, and the difference between the two.

		Sound Power (dB)		
		ISO 3741	VBRM	Difference
Third octave band by centerband frequency (Hz)	100	26.0	27.4	(1.4)
	125	21.9	21.8	0.1
	160	21.4	22.2	(0.8)
	200	24.9	24.6	0.3
	250	27.4	26.3	1.1
	315	30.8	29.9	0.9
	400	38.7	36.2	2.5
	500	54.6	52.4	2.2
	630	69.9	68.3	1.6
	800	77.5	75.8	1.7
	1,000	70.0	69.4	0.6
	1,250	64.1	64.4	(0.3)
	1,600	72.8	72.3	0.5
	2,000	69.8	70.3	(0.6)
	2,500	74.8	74.4	0.3
	3,150	71.3	72.2	(0.9)
	4,000	68.5	70.6	(2.1)
	5,000	69.0	71.1	(2.1)
	6,300	70.8	72.7	(1.9)
	8,000	73.4	74.8	(1.4)
	10,000	80.5	79.2	1.3
	Total	84.9	84.5	0.4

2.5 Conclusions

After a brief review of the concept of radiation resistance matrices and their uses, a derivation of the cylindrical radiation resistance matrix was presented. This produced a full, analytical expression for the matrix, which can be used in sound power calculations. The radiation

modes computed from this matrix were shown to match multipole trends at low frequencies, as would be expected from canonical radiation modes for other geometries. Numerical methods to evaluate the non-closed form equations were presented.

Following the derivation of the cylindrical radiation modes, sound power was computed for analytical simply-supported shell velocities using the VBRM method with these cylindrical modes. This power was compared to that calculated by BEM, which is treated as a benchmark. These results showed very good agreement between 0 Hz and 4 kHz with slight discrepancies of less than 1.5 dB appearing in some higher bands.

Experimental surface velocity measurements were collected using an SLDV and the sound power was determined using the VBRM method and the cylindrical radiation modes. The sound power was also measured using ISO 3741. These experimental results showed good agreement through the 10 kHz one-third-octave band. Between the 200 Hz and 10 kHz one-third octave bands the mean difference in the sound power obtained using ISO 3741 and the VBRM method was 0.1 dB with a standard deviation of 1.4 dB. The maximum difference between the two methods in any one-third octave band was 2.5 dB which occurred at the 400 Hz one-third octave band.

The results of the numerical simulations and the experimental work presented in this paper have shown that the cylindrical radiation resistance matrix and the accompanying acoustic radiation modes developed in the paper, implemented into the VBRM method, are useful tools which allow for the sound power measurement of cylinders. In addition, we see that modes developed for cylinders with infinite cylindrical baffles can accurately compute power for finite unbaffled cylinders.

Chapter 3

Frequency Trends of Cylinder Radiation Modes

3.1 Introduction

Acoustic radiation modes form an orthogonal basis that describes the radiation of sound from a surface velocity distribution. These modes have long been present in the search for a meaningful connection between vibration patterns and the resulting acoustic radiation, but they are less often utilized than the more popular methods of wavenumber filtering and structural-mode-based analysis. In contrast to structural modes, the radiation modes do not depend on the material or mounting conditions of the vibrating structure, but only on the geometry of the fluid-structure interface. They also orthogonalize the radiation operator, meaning that they radiate sound power independently of one another, while structural modes exhibit coupling in the generation of sound power. Radiation modes originally found use in active structural acoustic control as a metric for reducing total sound power;[5] because each radiation mode radiates sound power independently, minimizing vibration in one radiation mode invariably lowers the total sound power radiated.

More recently, radiation modes have been investigated as a method of calculating sound power from experimental vibration measurements,[3] as basis functions for acoustical holography,[13] and as design parameters for quieter structures.[12]

Though not originally known by their current name, radiation modes were first introduced in the literature in the early 1990s through three papers published within a year of each other. Photaidis first published a paper on the relationship between radiation modes and wavenumber filtering,[6] though he cited Borgiotti as the first to employ the modes. Borgiotti's paper came two months later, focusing on the relationships between radiation modes and the radiated sound power.[1] The third paper, by Sarkissian, introduced a simpler way to calculate radiation modes by eigenvector decomposition of the radiation resistance matrix;[14] this is the method commonly used today. Both Sarkissian and Photaidis were clear that radiation modes tend to have a preferential or peak wavenumber and that at high enough acoustic wavenumber k, the radiation modes with peak wavenumbers nearest to k tended to be the most efficient radiators of power. This was shown by examples at various frequencies.

At the present state of the literature, analytical formulations for the acoustic radiation modes, or the radiation resistance matrix from which they are derived, exist for two structure-fluid interface geometries, namely flat plates in infinite baffles and spheres. All other modes must be calculated through the means of boundary integral equations or the boundary element method, as described in Ref. 13. This requires significantly more computational power than the simple evaluation of expressions for the modes, especially if modes are needed over a large frequency range. Computational demands of radiation mode calculations could be minimized through additional analytical expressions for modes, as well as through better characterization of mode

trends over frequency. Efforts in this latter regard have recently been undertaken for sphero-cubic structures,[19] and the current work attempts to further develop such characterizations.

This chapter presents a formulation for the radiation resistance matrix of cylindrically curved objects. The matrix is formulated in terms of the cylindrical eigenfunctions of the wave equation. The resulting radiation modes are presented along with insight into their trends with frequency. Not only are the features noted by Photaidis and Sarkissian observed again here, but the trends of these features as the frequency is varied are investigated. It is found that the modes morph to meet the requirement that the most efficient modes must have peak wavenumber close to k. In addition, Sarkissian and Photaidis investigated only the axial dependence of radiation modes with axial symmetry, but here the full two-dimensional cylinder modes are shown, and the effects of the azimuthal dependence is shown in both wavenumber and physical domains.

3.2 Methods

The radiation resistance matrix is derived from the expression for sound power radiated from a vibrating structure. Given the acoustic pressure $\tilde{p}$ and the normal structure velocity $\tilde{u}$, the sound power may be calculated as

$$\Pi = \frac{1}{2}\mathrm{Re}\left\{\int_S \tilde{p}^*\tilde{u}\, dS\right\}, \tag{3-1}$$

where S is the surface of the vibrating structure, and $(\cdot)^*$ denotes the complex conjugate. If the vibrating structure is discretized into N discrete radiators of equal area, this may be rewritten in vector form as

$$\Pi = \frac{S}{2N}\mathrm{Re}\{\vec{p}^H\vec{u}\} \tag{3-2}$$

where $\vec{p}$ and $\vec{u}$ are $1 \times N$ vectors containing the acoustic pressure and normal surface velocity, respectively, evaluated at each surface point, and $(\cdot)^H$ indicates the Hermitian transpose. Because the pressure can be written in terms of the surface velocity through Green's functions, it is possible to write the power in terms of the surface velocities only as

$$\Pi = \frac{S}{2N} \mathrm{Re}\{\vec{u}^H \boldsymbol{Z} \vec{u}\} = \frac{S}{2N} \vec{u}^H \mathrm{Re}\{\boldsymbol{Z}\} \vec{u}, \tag{3-3}$$

where $\boldsymbol{Z}$ is the matrix of Green's functions between each pair of locations. The radiation resistance matrix is then defined as

$$\boldsymbol{R} = \frac{S_e}{2} \mathrm{Re}\{\boldsymbol{Z}\}, \tag{3-4}$$

with $S_e = S/N$ being the area of a single discrete radiator. Therefore, the derivation of the radiation resistance matrix is as simple as finding the Green's function between surface points.

This chapter presents eigenfunction decomposition formulations for the radiation resistance matrix of cylindrically curved objects in separable geometries. These geometries, shown in Fig. 3-1, include a full cylinder of finite length on an infinite cylindrical baffle, as in Fig. 3-1(a); a partial cylinder on an infinite cylindrical baffle, as shown in Fig. 3-1(b); and a partial cylinder radiating into a partial cylindrical space of extent θ_L, as shown in Fig 3-1(c). In each of these figures, grey surfaces are presumed to continue out to infinity.

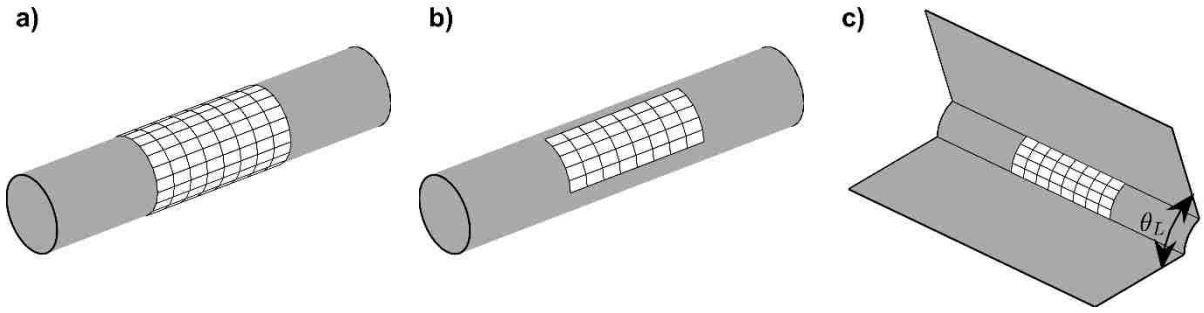

Figure 3-1: Cylindrical structures treated in this work. (a) A finite cylinder on an infinite cylindrical baffle. (b) A partial cylinder on an infinite cylindrical baffle. (c) A partial cylinder radiating into a partial cylindrical space of θ-extent θ_L.

The derivation is as follows: The eigenfunction decomposition in cylindrical coordinates allows the pressure field generated by the vibration of one discrete element to be expressed in the form

$$p(r,\theta,z) = \sum_{m=0}^{\infty} \int_0^{\infty} dk_z \, (A_m \cos m\theta + B_m \sin m\theta) \times (D(k_z) \cos k_z z + E(k_z) \sin k_z z) H_m^{(2)}(k_r r) \tag{3-5}$$

where m and k_z are separation constants, $k_r = \sqrt{k^2 - k_z^2}$, and $A_m, B_m, D(k_z)$, and $E(k_z)$ are constants to be determined. The velocity when one discrete element of the structure is vibrating may be approximated with a point source of equivalent source strength. Then, expanding the point source in terms of the θ and z eigenfunctions, and applying Euler's equation at the surface of the structure, we can find that the ijth element of the radiation resistance matrix for the first two structures in Fig. 3-1 is

$$R_{ij} = \frac{\omega \rho_0 S_e^2}{a\pi^2} \sum_{m=0}^{\infty} \cos\left(m\Delta\theta_{ij}\right) \int_0^k \mathrm{Im}\left\{\frac{H_m^{(2)}(k_r a)}{k_r H_m^{(2)'}(k_r a)}\right\} \cos\left(k_z \Delta z_{ij}\right) dk_z, \tag{3-6}$$

where a is the radius of the cylinder, ω is the angular frequency, ρ_0 is the density of air, and $\Delta\theta_{ij}$ and Δz_{ij} are the difference in θ position and z position of the ith and jth discrete elements. For the structure in Fig. 3-1(c) there are homogeneous Neumann boundary conditions at $\theta = 0, \theta_L$ instead of a periodicity condition. Thus the finished expression is

$$R_{ij} = \frac{\omega \rho_0 S_e^2}{\pi a \theta_L} \sum_{m=0}^{\infty} \cos\left(\frac{m\pi\theta_i}{\theta_L}\right) \cos\left(\frac{m\pi\theta_j}{\theta_L}\right) \int_0^k \mathrm{Im}\left\{\frac{H_{m\pi/\theta_L}^{(2)}(k_r a)}{k_r H_{m\pi/\theta_L}^{(2)'}(k_r a)}\right\} \cos\left(k_z \Delta z_{ij}\right) dk_z, \tag{3-7}$$

where θ_i and θ_j are the θ positions of the ith and jth discrete elements.

The radiation resistance matrices in Eqs. (3-6) and (3-7) may be used for power calculations as in Eq. (3-3), or they may be decomposed into the radiation modes. Eigendecomposition of these matrices gives eigenvectors $\{\boldsymbol{q}_r\}$, which are the radiation modes, and eigenvalues $\{\lambda_r\}$, which are proportional to the radiation efficiencies of the associated modes. The radiation modes are presented in the following section at various kL values for a cylinder with $L/a = 6$ and with a θ extent of $\pi/2$ for the partial cylinders.

In addition to simply looking at the radiation modes themselves, the following results include wavenumber transforms of the radiation modes for a full cylinder. Because the radiation modes are real, the magnitude of the wavenumber transforms will be symmetrical across the axes; thus only the first quadrant of the wavenumber domain is shown. The radiation modes are padded by many zeros above and below the mode in the z direction to represent the rigid baffle, after which a two-dimensional fast Fourier transform is used. These transforms allow us to look for the trends that Sarkissian and Photaidis mentioned as the frequency varies.

3.3 Results

The first nine radiation modes for each geometry are shown in Fig. 3-2 for $kL \ll 1$, sorted by radiation efficiency, with parts (a)-(c) corresponding to the geometries presented in Fig. 3-1, parts (a)-(c). For each geometry, there is a multipole-like pattern in the series of modes: The first mode is a breathing, or monopole mode, the next two or three modes feature two out of phase regions like a dipole, the few after that resemble longitudinal or lateral quadrupoles, and so on. This similarity can also be seen in a plot of the efficiencies, given for the full cylinder modes in Fig. 3-3; below about $kL = 0.5$ rad the monopolar modes follow a 6 dB/octave increase, the dipolar modes follow a 12 dB/octave trend, and the quadrupolar modes increase at 18 dB/octave. It is interesting to note that the mode shapes for the partial cylinders on a cylindrical baffle and

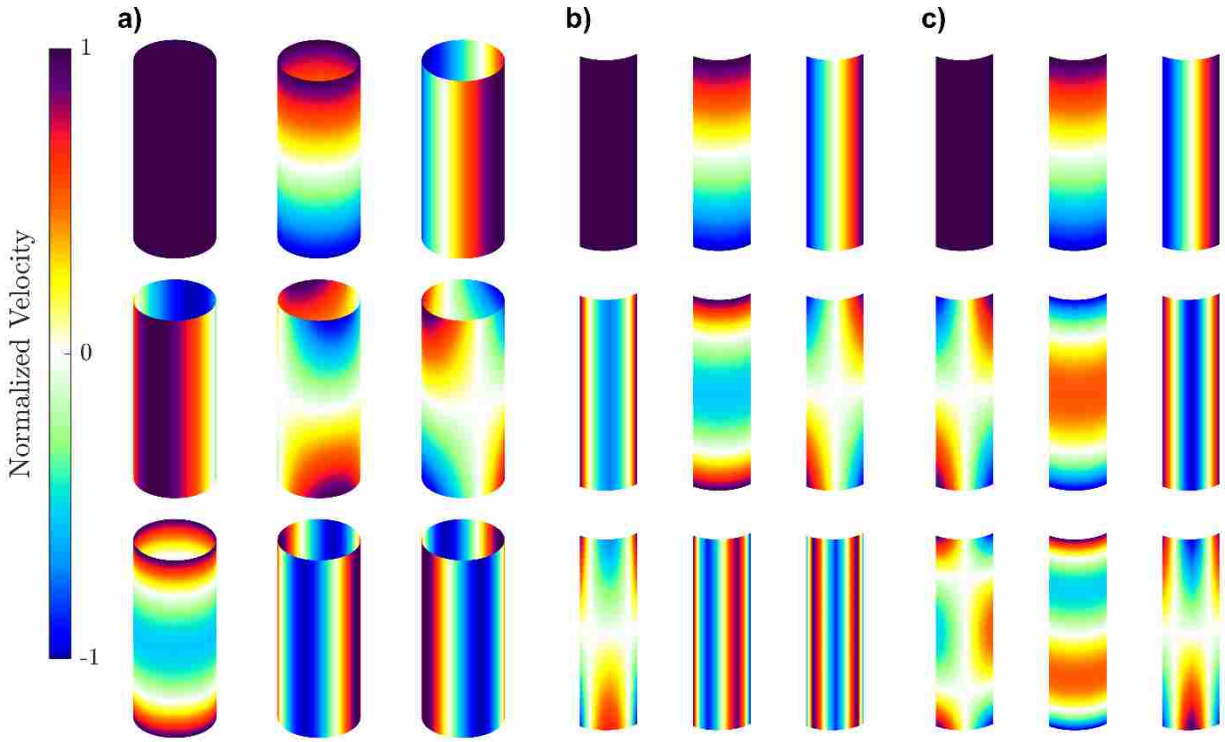

Figure 3-2: The nine most efficient acoustic radiation modes for each of the three geometries in Fig. 3-1. (a) Full cylinders, (b) Partial cylinders on a cylindrical baffle, (c) partial cylinders radiating into a quarter space.

those for partial cylinders radiating into a partial space are very similar at this low kL. Some of the modes switch places in the lineup of efficiency, and there are slight differences in those that match, but the general shapes are the same.

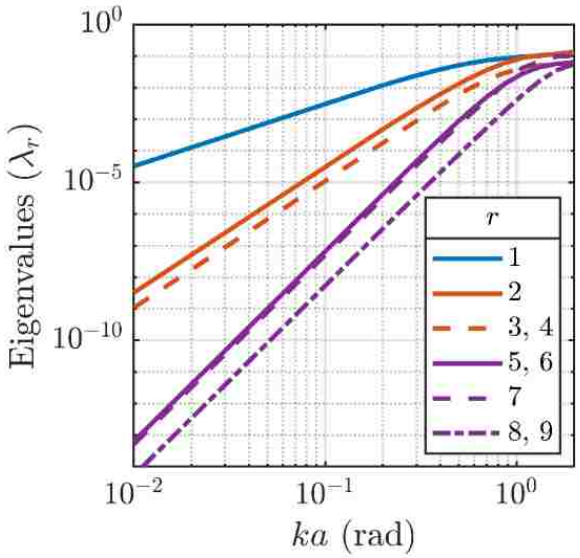

Figure 3-3: Efficiencies of the few most efficient full cylinder modes at low kL**. The multipole-like effects can be seen in the rate of increase of these efficiencies with frequency.**

Next we turn to the wavenumber transforms of the full cylinder modes. Initial wavenumber transforms of the most efficient modes with zero-order, first-order, and second-order θ dependence are shown in Fig. 3-4 for $kL = 6$. It is seen that each mode has only one wavenumber component in the θ direction, corresponding to the order of the θ dependence. In other words, the θ dependence of each of the modes is purely sinusoidal. All wavenumber transforms for the balance of this paper will therefore be presented as line plots, showing the k_z dependence for only the k_θ value at which the transform is non-zero.

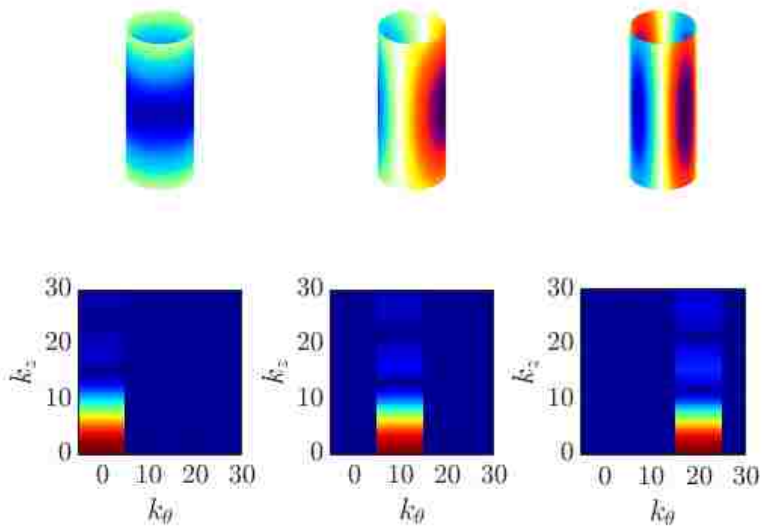

Figure 3-4: The most efficiently radiating modes with zero-order, first-order, and second-order θ dependence, and their associated 2D wavenumber transforms.

These line plots are shown in Fig. 3-5 for the four most efficient modes (from left to right) with no θ dependence. Here we begin to look at trends with frequency, as the same four modes are shown at several kL values. In Fig. 3-5(a) the first four modes each peak at a different wavenumber, but as the acoustic wavenumber increases from $kL = 6$ to $kL = 9$ in Fig. 3-5(b), it is seen that the first two modes peak around the same k_zL, and the third mode has shifted to a peak wavenumber at $k_zL = 0$. As the frequency continues to increase, the first two modes peak at around the same wavenumber, which closely follows the acoustic wavenumber, and the third and fourth mode begin to peak at the same wavenumber as well, which follows after the more efficient modes' peak wavenumber.

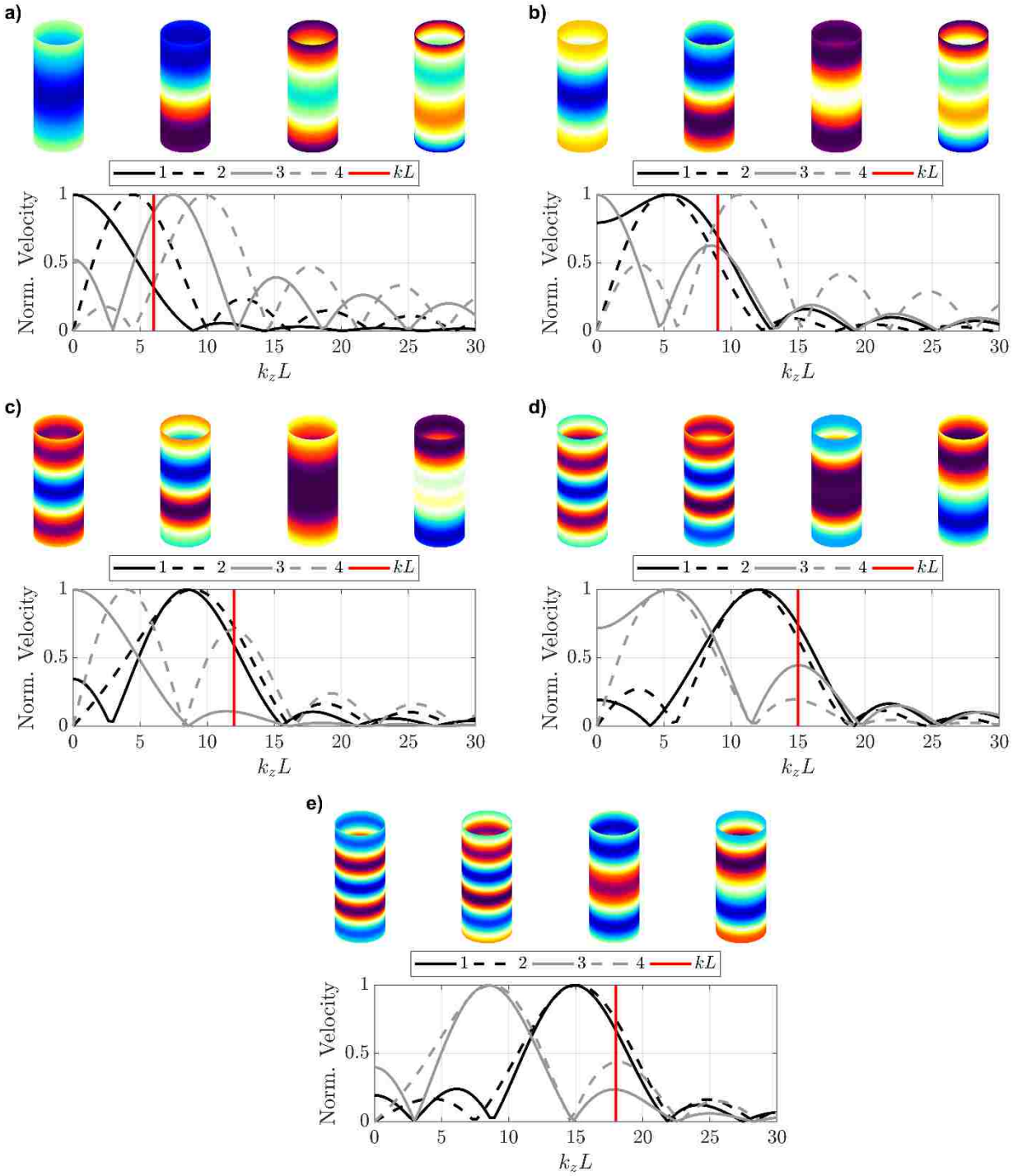

Figure 3-5: The physical space and wavenumber space representations of the first four radiation modes with no θ dependence. (a) at $kL = 6$. (b) at $kL = 9$. (c) at $kL = 12$. (d) at $kL = 15$. (e) at $kL = 18$.

In other words, pairs of modes emerge that have the same or similar peak wavenumbers. The peak wavenumbers of the most efficient pair follow the acoustic wavenumber, and each

subsequent pair of modes has a peak wavenumber that follows that of the pair before. In each pair of modes there is one mode which has even symmetry about the center of the structure's z-extent and one which has odd symmetry about that center. As the modes morph to higher wavenumbers, these symmetries do not change. It is interesting as well to look at the efficiencies of these pairs of modes at high kL. Shown in Fig. 3-6 are the efficiencies of the four modes whose trends are given in Fig. 3-5. It can be seen that at high enough kL the two modes with similar peak wavenumbers also have similar efficiencies. These efficiencies constantly leapfrog each other as the wavenumbers increase, but the pairs with no θ dependence do not overtake each other in efficiency. This means that the two most efficient modes will always be the two most efficient modes at high kL.

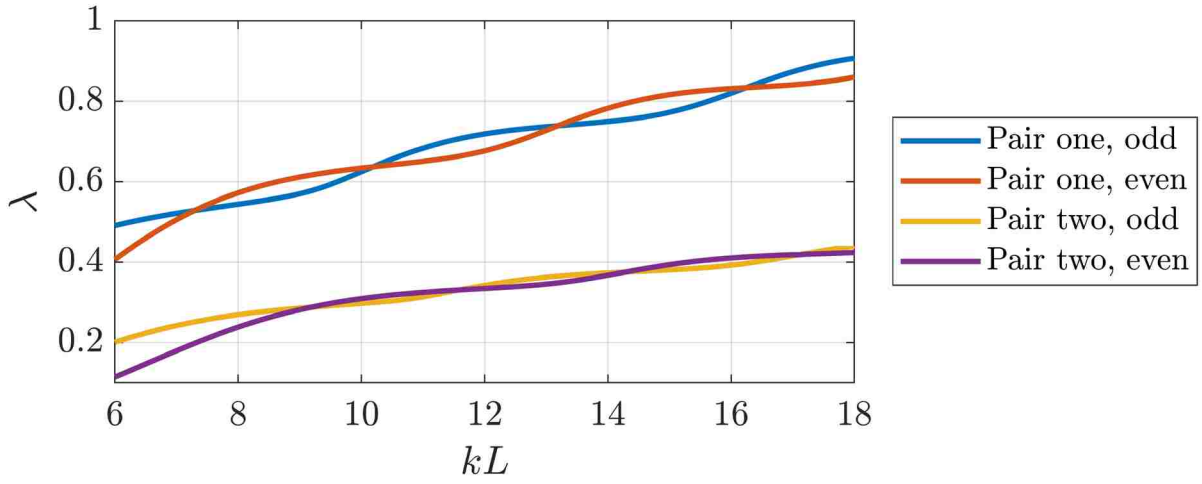

Figure 3-6: Efficiency of the first few modes with zero-order and first-order θ dependence at high kL

The trends above are also exhibited in modes with first-order or second-order θ dependence, though with a slight variation. Figure 3-7 shows the four most efficient modes with second-order θ dependence at $kL = 18$, which corresponds to Fig. 3-5(e). These modes come in degenerate pairs; the first two modes have identical efficiencies and wavenumber transform magnitudes, as do the last two shown. The difference between the first and second (and between

the third and fourth) modes is simply a $\sin 2\theta$ versus a $\cos 2\theta$ dependence. As such, all four of these modes become a peak wavenumber "pair" in which the peak wavenumbers are similar and change together with frequency. The wavenumber transforms shown here make obvious an important point; these most efficient modes with second-order θ dependence do not follow the acoustic wavenumber, but rather the effective acoustic wavenumber given by $\sqrt{k^2 - k_\theta^2}$, also known as the radiation circle.

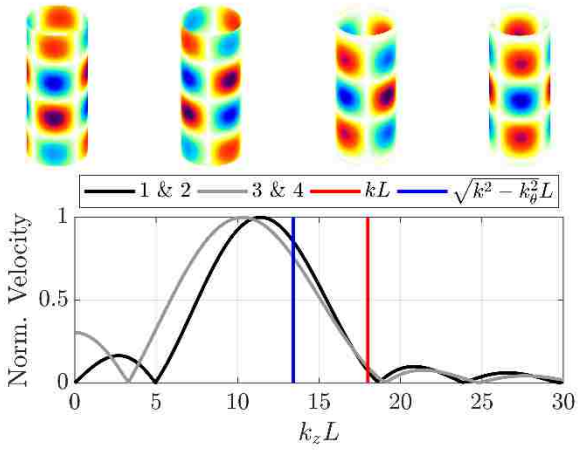

Figure 3-7: The physical space and wavenumber space representations of the first four radiation modes with second-order θ dependence at $kL = 18$.

3.4 Discussion

As has been shown above, the most efficient radiation modes have peak wavenumbers that tend to follow the radiation circle as it moves with frequency. This is true regardless of the circumferential wavenumber of the modes. While k_z changes with frequency in this case, k_θ does not. Similar analysis of the other structures given in Fig. 3-1 show that this morphing effect occurs in the z dimension for all three mode types, but in the θ dimension only for the partial cylinders

on an infinite cylindrical baffle. Comparison with other known radiation modes, such as those for flat baffled plates and those for spheres, suggests that this morphing of radiation modes with frequency occurs only in dimensions where the structure does not span the whole dimensional space. For example, a vibrating sphere covers the whole ϕ and θ dimensions over which the fluid-structure interface is defined, and consequently there is no variation of the radiation modes with frequency. In contrast, the radiation modes of flat plates morph with frequency in both dimensions over which they are defined; this is because the flat plate does not cover the full breadth of either of those dimensions.

Chapter 4

Radiation Modes for Curved Plates

4.1 Introduction

Acoustic radiation modes (ARM) are an orthogonal basis for sound radiation from structures. First introduced in the 1990s,[1,6,14] these modes are the eigenvectors of the radiation resistance matrix, and thus they radiate sound power independently. While structural modes must satisfy the differential equations and boundary conditions describing the vibration of a structure, radiation modes are boundary condition and material independent and depend only on the geometry of the structure-fluid interface. ARM have found widespread use in active structural acoustic control, as the lack of intermodal coupling makes the radiation mode amplitudes a straightforward choice of control parameter.[5] In more recent years, they have also been used as basis functions in near-field acoustical holography,[13] as guides in structure modifications for noise reduction,[12] and in experimental measurement of sound power.[3]

Though ARM are widely useful, analytical expressions for the modes, or for the radiation resistance matrices from which they are derived, exist for only a few geometries. Radiation resistance matrices for baffled flat plates can be expressed in terms of a discretized Rayleigh integral,[5] and the radiation modes for spherical geometries are known to be the spherical harmonics.[6] ARM for almost all other geometries are typically calculated using the boundary element method or boundary integral equations. These methods require significantly more computational power than evaluation of the expressions for flat plates and spherical geometries. It is desirable, therefore, to develop analytical expressions for more geometries.

Recently, studies have developed radiation resistance matrices for cylinders using eigenfunction expansion, and these add one additional geometry to the list of analytical expressions. Aslani et al. developed the matrix for a cylinder sandwiched between two infinite pressure release planes using this technique,[16] and Goates et al. recently produced a similar formulation for cylinders on infinite cylindrical baffles, given in Chapter 2. Other studies have considered radiation modes for cylindrical objects,[1,6,14,15] but these were developed using boundary element or boundary integral formulations.

This work presents an additional formulation for radiation resistance matrices of cylindrically curved structures, based on the uniform theory of diffraction.[20] This formulation relies on high-frequency asymptotes to simplify the eigenfunction expansion expressions, and was originally developed for electromagnetic radiation. Rather than expanding the field in terms of eigenfunctions, this theory represents the field in terms of geometrical rays, and simplifies to flat plate expressions at zero curvature. An additional benefit of this formulation is the potential generalizability to other structures with non-cylindrical or non-constant curvature, as has been done in the electromagnetic radiation developments of the theory.

This chapter will also investigate the applicability of both the eigenfunction and diffraction-based cylinder modes to a baffled curved plate. This structure geometry does not exactly match the geometries modeled by the modes given here, but it approaches more closely structures that may be encountered in experimental situations. This will indicate how well these modes can be extended to approximately cylindrical cases.

4.2 Theory

The radiation resistance matrix is derived from the pressure that a small vibrating element of a structure generates across the structure. In practice the structure is divided into several discrete patches, and the pressure is evaluated at each of these locations. Once this pressure is known for arbitrary location of the vibrating element, the ijth element of the radiation resistance matrix is calculated as

$$R_{ij} = \frac{S_e}{2u_0}\mathrm{Re}\{p_i(a, \theta_j, z_j)\} \tag{4-1}$$

where u_0 is the amplitude of the vibration, S_e is the area of the vibrating element, $p_i(r, \theta, z)$ is the pressure generated by vibration at the ith location, and θ_j, z_j are the coordinates of the jth location. This derivation is summarized below for previously published eigenfunction expansion formulations, after which the diffraction-based formulation is derived.

4.2.1 Eigenfunction Expansion

Consider a hard infinite cylinder of radius a, and assume that a small rectangular patch of the cylinder with θ extent $\Delta\theta$ and height Δz is vibrating with velocity u_0, such that there is effectively a simple source of strength $u_0 a \Delta\theta \Delta z$ at $(r, \theta, z) = (a, \theta_j, z_j)$. This vibration creates a pressure field that can be written as

$$p_j(r,\theta,z) = \sum_{m=0}^{\infty} \int_0^{\infty} dk_z \, (A_m \cos m\theta + B_m \sin m\theta) \times (D(k_z) \cos k_z z + E(k_z) \sin k_z z) H_m^{(2)}(k_r r), \tag{4-2}$$

where $k_r = \sqrt{k^2 - k_z^2}$, k is the wavenumber, k_z is the axial wavenumber, m is the θ index, $H_m^{(2)}(x)$ is the mth-order Hankel function of the second kind, and A_m, B_m, $D(k_z)$, and $E(k_z)$ are coefficients yet to be determined. The surface velocity may be expanded in terms of the θ and z eigenfunctions as

$$u_j(\theta,z) = \frac{u_0 \Delta\theta \Delta z}{\pi^2} \sum_{m=0}^{\infty} \left(\cos m\theta_j \cos m\theta + \sin m\theta_j \sin m\theta\right) \times \int_0^{\infty} \left(\cos k_z z_j \cos k_z z + \sin k_z z_j \sin k_z z\right) dk_z, \tag{4-3}$$

after which pressure expression coefficients may be solved for by applying the surface condition

$$\left.\frac{\partial p_j}{\partial r}\right|_{r=a} = -j\rho_0 \omega \, u_j(\theta,z), \tag{4-4}$$

where the non-subscripted $j = \sqrt{-1}$. Applying these steps and simplifying gives the pressure as

$$p_j(r,\theta,z) = -j \frac{u_0 \rho_0 \omega \Delta\theta \Delta z}{\pi^2} \sum_{m=0}^{\infty} \left(\cos m\theta_j \cos m\theta + \sin m\theta_j \sin m\theta\right) \times \int_0^{\infty} \left(\cos k_z z_j \cos k_z z + \sin k_z z_j \sin k_z z\right) \frac{H_m^{(2)}(k_r r)}{k_r H_m^{(2)\prime}(k_r a)} dk_z \tag{4-5}$$

$$= -j \frac{u_0 \rho_0 \omega \Delta\theta \Delta z}{\pi^2} \sum_{m=0}^{\infty} \cos\left[m(\theta - \theta_j)\right] \int_0^{\infty} \frac{H_m^{(2)}(k_r r)}{k_r H_m^{(2)\prime}(k_r a)} \cos\left[k_z(z - z_j)\right] dk_z.$$

Substituting this into Eq. (4-1) gives the ijth element of the radiation resistance matrix as

$$R_{\text{cyl},ij} = \frac{S_e}{2u_0}\text{Re}\{p_j(a,\theta_i,z_i)\}$$

$$= \frac{S_e^2\omega\rho_0}{a\pi^2}\sum_{m=0}^{\infty}\cos[m(\theta_i-\theta_j)]\int_0^k \frac{1}{k_r}\text{Im}\left\{\frac{H_m^{(2)}(k_r a)}{H_m^{(2)'}(k_r a)}\right\}\cos[k_z(z_i-z_j)]\,dk_z, \quad (4\text{-}6)$$

where the substitution $S_e = a\Delta\theta\Delta z$ has been made.

In addition to this full cylinder expression, eigenfunction expansion can give the radiation resistance matrix for a partial cylinder radiating into a partial cylindrical space, such as a half cylinder on an infinite baffle radiating into a half space. The formulation for this situation is similar; the main difference is the application of a Neumann boundary condition at $\theta = 0$ and $\theta = \theta_L$, where θ_L is the angular extent of the space, instead of the periodicity requirement on θ. Making these changes yields a very similar expression, with

$$R_{\text{partcyl},ij} = \frac{S_e^2\omega\rho_0}{a\pi\theta_L}\sum_{m=0}^{\infty}\cos\frac{m\pi\theta_i}{\theta_L}\cos\frac{m\pi\theta_j}{\theta_L}\int_0^k \frac{1}{k_r}\text{Im}\left\{\frac{H_{m\pi/\theta_L}^{(2)}(k_r a)}{H_{m\pi/\theta_L}^{(2)'}(k_r a)}\right\}\cos[k_z(z_i-z_j)] \quad (4\text{-}7)$$

4.2.2 Uniform Theory of Diffraction

The second type of radiation mode formulation undertaken here is based on the uniform theory of diffraction (UTD). This approach to wave propagation around curved surfaces was first developed in electromagnetics,[20,21,22] but has found limited use in acoustics.[23] This formulation can be derived using an asymptotic expansion of Eq. (4-5) for large ka. Equation (4-5) can be written in a slightly different form after evaluation at $r = a$ as

$$p_j(a,\theta,z) = -j\frac{u_0\rho_0\omega\Delta\theta\Delta z}{4\pi^2}\int_{-\infty}^{\infty}dk_z\frac{e^{jk_z(z-z_j)}}{k_r}\sum_{m=-\infty}^{\infty}\frac{H_m^{(2)}(k_r a)}{H_m^{(2)'}(k_r a)}e^{jm(\theta-\theta_j)}. \quad (4\text{-}8)$$

The sum in this expression can be transformed using a Watson transformation,[21] as follows (substituting $\phi = \theta - \theta_j$):

$$\sum_{m=-\infty}^{\infty} \frac{H_m^{(2)}(k_r a)}{H_m^{(2)'}(k_r a)} e^{jm\phi} = \frac{j}{2}\int_C \frac{e^{j\nu(\phi-\pi)}}{\sin \nu\pi} \frac{H_\nu^{(2)}(k_r a)}{H_\nu^{(2)'}(k_r a)} d\nu$$
$$= \frac{j}{2}\int_{-\infty-j\varepsilon}^{\infty-j\varepsilon} \frac{\cos \nu(\phi-\pi)}{\sin \nu\pi} \frac{H_\nu^{(2)}(k_r a)}{H_\nu^{(2)'}(k_r a)} d\nu, \quad (4\text{-}9)$$

where C is a contour that encircles the real axis, and the last equality comes by replacing $-\nu$ by ν in the part of the contour above the axis. If the trigonometric functions are replaced by their exponential equivalents, employment of a geometric series yields

$$\sum_{m=-\infty}^{\infty} \frac{H_m^{(2)}(k_r a)}{H_m^{(2)'}(k_r a)} e^{jm\phi} = \frac{j}{2}\int_{-\infty-j\varepsilon}^{\infty-j\varepsilon} d\nu \frac{H_\nu^{(2)}(k_r a)}{H_\nu^{(2)'}(k_r a)} \sum_{\ell=0}^{\infty} \left(e^{-j\nu(2\pi-\phi)} + e^{-j\nu\phi}\right) e^{-j2\pi\ell\nu}. \quad (4\text{-}10)$$

The left-hand side of Eq. (4-10) can be interpreted as a summation of waves which have encircled the cylinder ℓ times, with one set of terms for those circling in a positive direction and one set for those in the negative direction. This becomes more apparent after noting that the primary contribution to the integral over ν is at $\nu = k_r a$; Pathak et al. suggest the substitution $\nu = k_r a + \tau(k_r a/2)^{1/3}$, making τ the new independent variable.[24] If it is assumed that ka—and by extension $k_r a$—is large enough, only the $\ell = 0$ terms contribute significantly to the pressure and all but the first term in the summation can be dropped.[24] Employing this assumption, and following the asymptotic formulation of Pathak et al., Eq. (4-8) can be rewritten as

$$p_j(r,\theta,z) = -\frac{u_0\rho_0\omega\Delta\theta\Delta z}{8\pi^2}\int_{-\infty}^{\infty} dk_z \frac{e^{j[k_z(z-z_j)+k_r a\phi]}}{k_r}\int_{-\infty}^{\infty} d\tau \sqrt[3]{\frac{k_r a}{2}}\frac{W_2(\tau)}{W_2'(\tau)} e^{-j\sqrt[3]{\frac{k_r a}{2}}\tau}, \quad (4\text{-}11)$$

after which a polar transformation allows the first integral to be evaluated, resulting in the expression for the pressure from one ray being written as

$$p_j(t) = \frac{j\rho_0 \omega u_0 S_e}{2\pi} V(\xi) \frac{e^{-jkt}}{t}, \tag{4-12}$$

where

$$V(\xi) = \sqrt{j\xi/4\pi} \int_{-\infty}^{\infty} d\tau \frac{W_2(\tau)}{W_2'(\tau)} e^{-j\xi\tau}, \tag{4-13}$$

$\xi = t(k\cos^2\psi/a^2)^{1/3}$, $t = \sqrt{\Delta z^2 + a^2\Delta\theta^2}$ is the distance traversed across the curved surface, and $\psi = \tan^{-1}\frac{\Delta z}{a\Delta\theta}$ is the angle between the direction of propagation and the cylinder axis. Substitution of Eq. (4-12) into Eq. (4-1) gives the expression for elements of the radiation resistance matrix for a curved plate as

$$R_{\text{curved},ij} = -\frac{\rho_0 \omega S_e^2}{4\pi d_{ij}} \text{Im}\{V(\xi) e^{-jkd_{ij}}\}. \tag{4-14}$$

where d_{ij} is the surface distance between the ith and jth positions on the surface, and d_{ij} is also substituted for t in ξ. Note that this only describes the radiation resistance with a single ray; this will work well for the situations treated in this work, but for treatment of a full cylinder one should use a combination of two terms of Eq. (4-14) to describe the two opposite paths around the cylinder from the source to the field point.

The function $V(\xi)$ may seem to pose a problem for evaluating these expressions, but it has been sufficiently characterized to produce useful series representations with ten terms or less, which are given in an appendix of Ref [20]. A plot of $V(\xi)$ is shown in Fig. 4-1; of note is the fact that at very low curvature or low frequency $\xi \to 0$, and $V(\xi) \to 1$. In this case, Eq. (4-14) collapses to the canonical expression for the radiation resistance matrix of a flat plate.

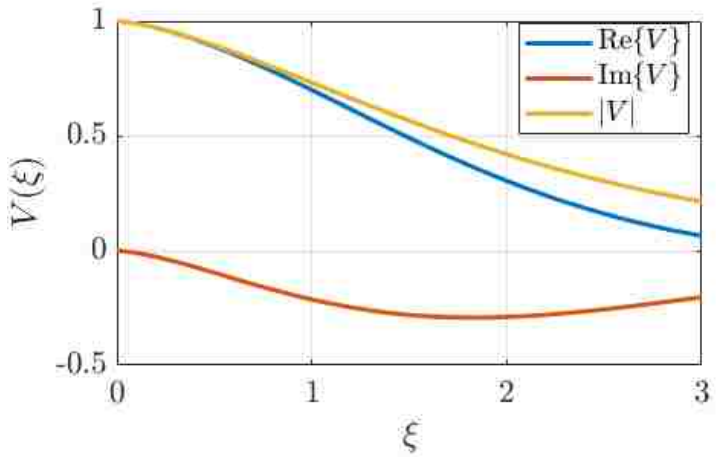

Figure 4-1: A plot of the function V(ξ), showing the real part, imaginary part, and magnitude of the function.

4.2.3 Flat Plate Expression

The similarities between flat plate and curved plate expressions for the pressure lead to a question: How dissimilar are the effects accounted for by the two? As such, the two mode formulations above will be compared to the radiation modes for a flat plate, given by

$$R_{\text{flat},ij} = \frac{\rho_0 \omega^2 S_e^2}{4\pi c} \frac{\sin k d_{ij}}{k d_{ij}}. \tag{4-15}$$

The treatment of full cylinders using a superposition of Eq. (4-14) with multiple d_{ij} suggests that perhaps the same can be done with the flat plate expression. Though full cylinders will not be treated in this work, the possibility of doing so using this expression is intriguing.

4.3 Radiation Mode Results

Radiation mode shapes corresponding to Eqs. (4-15), (4-6), and (4-7) are present in the literature; as such, the mode shapes corresponding to Eq. (4-14) are now shown in the context of comparison to some of these other modes. Figure 4-2 shows the few modes that are most efficient according to the cylinder formulation (Eq. (4-6)) and the curved plate formulation (Eq. (4-14)) for a cylindrically curved plate with curvature such that $ka = 4.5$ and dimensions $kL_x = 4.5$ and

$kL_y = 4.5$. Also shown are the most efficient flat plate modes mapped onto the same curved structure. The modes in this case are very similar, with the first four of each type being almost indistinguishable from each other. The fifth and sixth modes of each type seem to be slight variations on each other, and the seventh and eighth are almost identical, within a switching of order. At this kL, these are all the modes with efficiencies within the first two orders of magnitude.

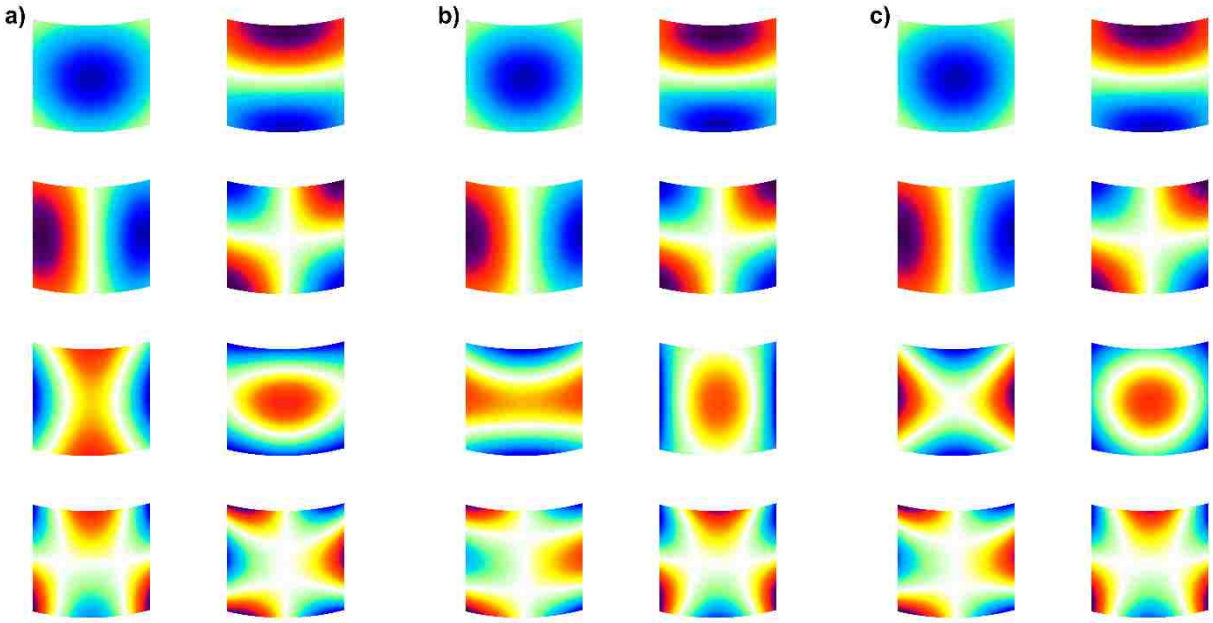

Figure 4-2: The eight most efficient modes for three different mode formulations on a square curved plate with kL = ka = 4.5. (a) The eigenfunction expansion cylinder modes. (b) The uniform theory of diffraction curved plate modes. (c) The canonical flat plate modes mapped to a curved plate surface.

To get a wider survey of when and how well the modes match each other, modes are compared using the modal assurance criterion. The modal assurance criterion (MAC) between modes a and b is calculated as

$$\mathrm{MAC}_{ab} = \frac{|\boldsymbol{q}_a \cdot \boldsymbol{q}_b|^2}{(\boldsymbol{q}_a \cdot \boldsymbol{q}_a)(\boldsymbol{q}_b \cdot \boldsymbol{q}_b)}, \tag{4-15}$$

where the dot indicates the dot product. This effectively takes the correlation of two modes, which will be 1 if they are identical and 0 if they are orthogonal. Modal assurance criteria were calculated for the first 15 radiation modes of each type on a 30.5 by 30.5 cm square plate curved to various radii of curvature a, from nearly flat at $a = 1$ m, to a half cylinder at $a = 9.7$ cm, and at frequencies from 200 Hz to 2000 Hz in steps of 200 Hz. An example heatmap of the MAC between cylinder modes and curved plate modes at 800 Hz for a radius of 30.5 cm is shown in Fig. 4-3; the first eight modes in each set are shown in Fig. 4-2(a) and Fig. 4-2(b). A MAC of one indicates that the modes are the same; a perfectly matched set of modes would have a MAC plot with ones on the diagonal, and zeros everywhere else. At low frequencies not all 15 modes are very efficient; it is found that there is very little correlation between modes of different types if the efficiency of one or both modes is below the first three orders of magnitude. In Fig. 4-3, only the first eight modes fit this condition. It is seen that the first four modes match with 90% MAC or greater, as do the seventh and eighth modes, though the order is switched. The fifth and sixth modes, however, are a bit of a crossover between the two mode types; each contains a bit of both the fifth and sixth modes of the other type, as is evident from Figs. 4-2(a) and 4-2(b).

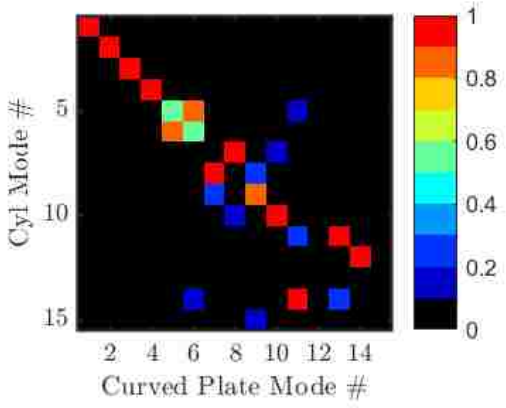

Figure 4-3: Modal assurance criteria calculated between the first 15 cylinder and curved plate modes for the geometry and frequency combination in Fig. 4-1, i.e., $\mathbf{f = 800}$ Hz, $\mathbf{a = 30.5}$ cm, and $\mathbf{L_x = L_y = a}$.

The MAC comparisons between the cylinder and curved plate modes are similar to Fig. 4-3 for many frequency/radius combinations, but other combinations exhibit different characteristics. At the low curvature of $a = 1$ m, all the MAC heatmaps follow the trends of the first eight modes of Fig. 4-3, i.e., the modes with efficiencies in the first three orders of magnitude match well. In addition, at 200 Hz for each curvature the MAC heatmap displayed similar characteristics to Fig. 4-3 with the two to three modes efficient enough to consider matching between the two formulations. As the curvature or frequency is increased, there is a region in this parameter space in which the modes display significant crossover; i.e., two or more modes of one formulation will correlate well to two or more modes of the other formulation. This is demonstrated by Fig. 4-4, which gives the MAC between the first 15 modes of the cylinder and curved plate modes at $f = 1000$ Hz, $a = 9.7$ cm: Cylinder modes 8 and 9 correlate well with both curved plate mode 6 and curved plate mode 10. In addition, in this figure, cylinder modes 11 and 13 both correlate with curved plate modes 12 and 13.

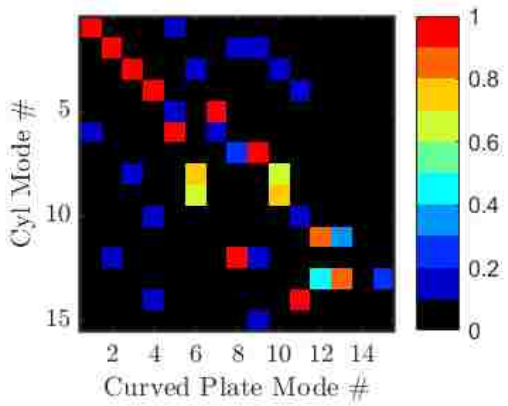

Figure 4-4: Modal assurance criteria calculated between the first 15 cylinder and curved plate modes for f = $1000\ Hz$, a = $9.7\ cm$, and $L_x = L_y = 30.5\ cm$.

One final example is shown in Fig. 4-5; at high curvature and frequency the MAC becomes very messy, with very few of the modes showing perfect correlation with each other. Figure 4-5

gives an example of this at the edge of the parameter range characterized here, with $f = 2000$ Hz, $a = 9.7$ cm. There are split correlations here, like there were in Fig. 4-4—for example, in Fig 4-5 cylinder modes 5 and 9 correlate somewhat with curved plate modes 4 and 5—but the heatmap is overall messier and harder to make sense of.

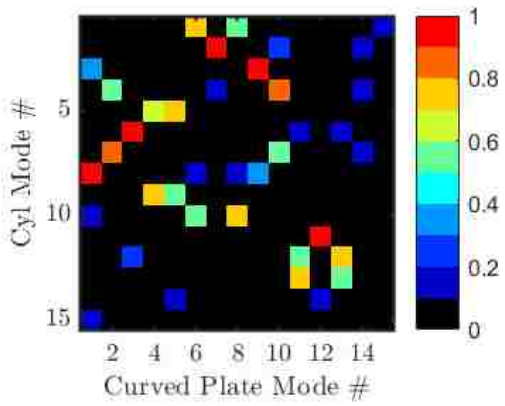

Figure 4-5: Modal assurance criteria between the first 15 cylinder and curved plate modes for $\mathbf{f = 2000\ Hz}$, $\mathbf{a = 9.7\ cm}$, and $\mathbf{L_x = L_y = 30.5\ cm}$.

From these MAC heatmaps and the plots of the first few modes in Fig. 4-2, we can see that the modes do match well or approximately in many areas, but they also diverge significantly in the high frequency, high curvature range of the parameter space.

4.4 Application to Sound Power

The cylinder, curved plate, and flat plate modes will now be employed to calculate sound power of a curved plate structure. These results will be compared to sound power calculations from the boundary element method. The structure under test is a 30.5 x 30.5 cm plate, curved to various radii of curvature, rigidly capped on the ends, and backed by an infinite baffle. An example of one configuration of this plate is shown in Fig. 4-6(a), where the grey plane continues off to infinity. Plate velocities are generated by a point force in a finite element simulation, and the

velocities are fed into the radiation modes routines, as well as a boundary element analysis routine. The finite element and boundary element analyses are performed in VibroAcoustics One, a commercial software package produced by the ESI Group.

Though none of the formulations match the geometry exactly, the sound power will be calculated using the radiation resistance matrices given in Eqs. (4-6), (4-7), (4-14), and (4-15), with $\theta_L = \pi$ in Eq. (4-7). The geometries these equations represent are shown in Fig. 4-6(b) through 4-6(e) for comparison with the true geometry. The sound power results are not shown directly, but in Fig. 4-7 the difference in dB between BEM and each radiation resistance matrix approach is shown, calculated as $\Delta L_{\Pi} = 10\log_{10}(\Pi_{\mathrm{RR}}/\Pi_{\mathrm{BEM}})$, where Π_{BEM} is the power from BEM, and Π_{RR} is the power calculated by the radiation resistance matrix under consideration.

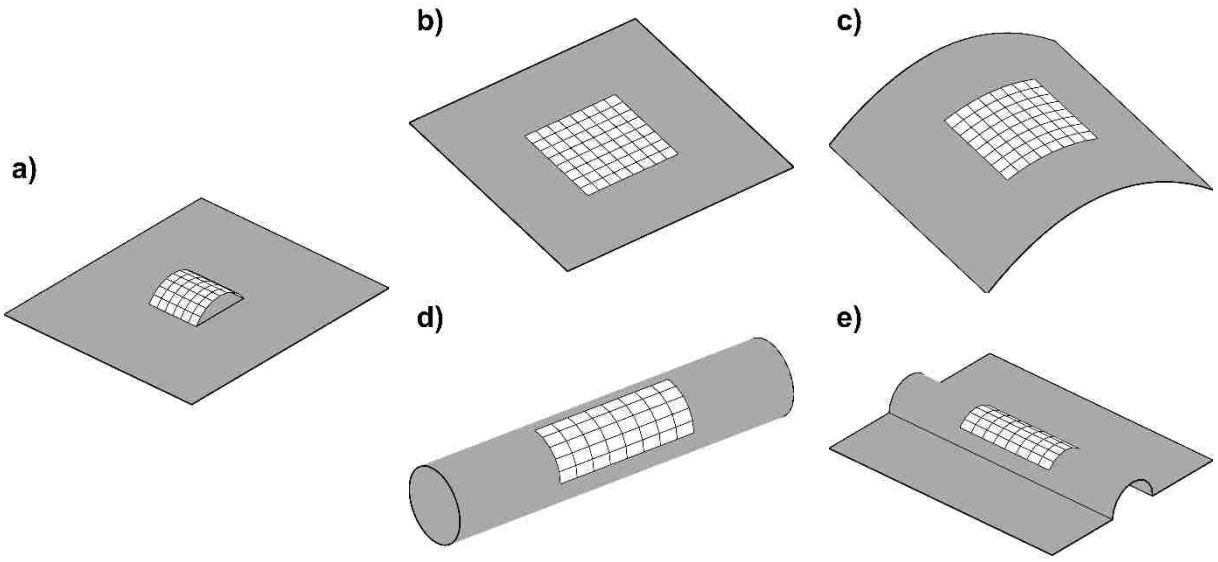

Figure 4-6: The geometry of the curved plate computational experiment and the radiation modes which will be used to approximate it. All grey surfaces are assumed to continue to infinity. (a) the geometry of the baffled curved plate experiment. (b) the flat plate geometry. (c) the curved plate geometry. (d) the cylinder geometry. (e) the baffled half cylinder geometry.

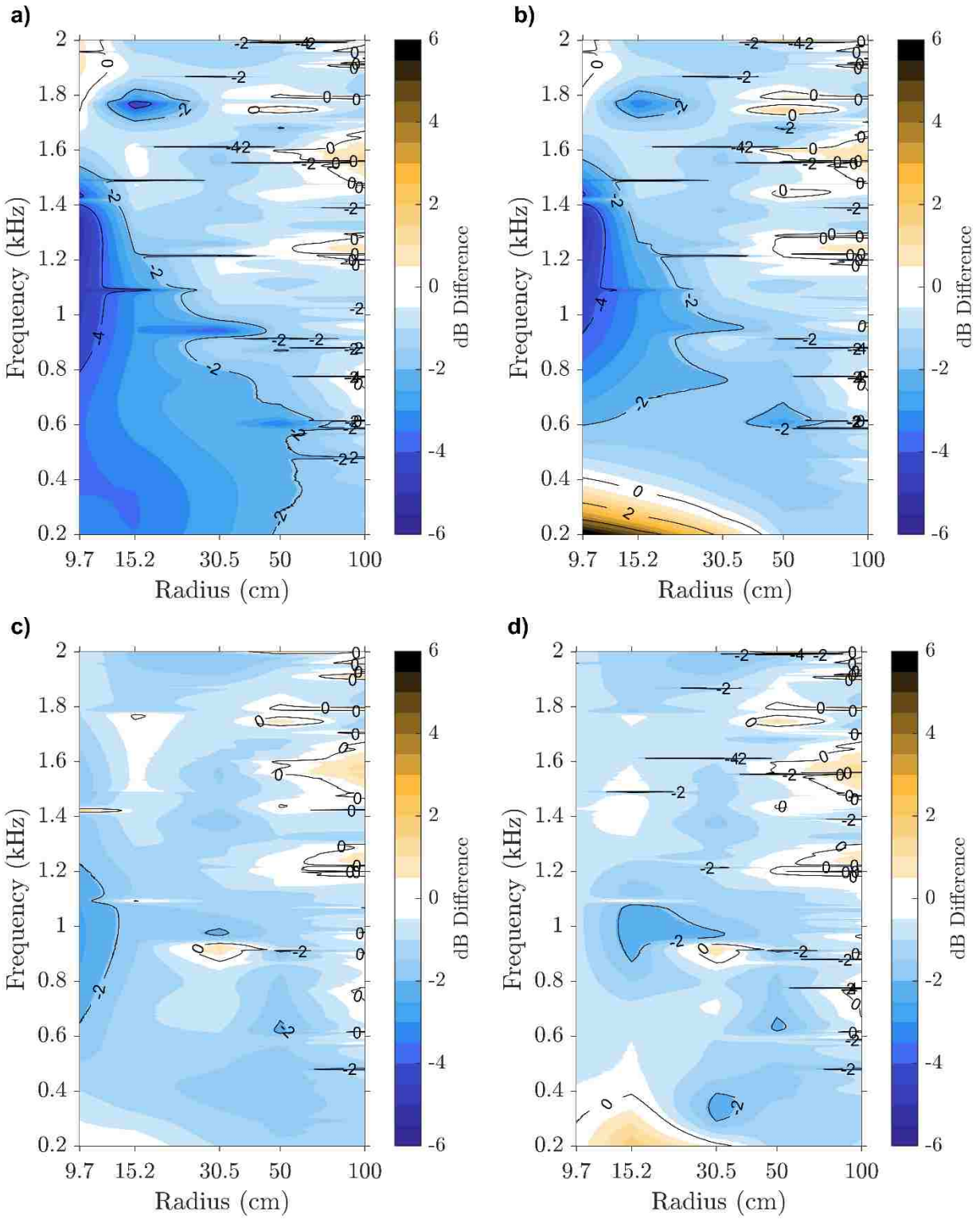

Figure 4-7: Difference between the radiation resistance approach and BEM for each of the following radiation resistance formulations: (a) flat plate radiation resistance. (b) curved plate radiation resistance. (c) full cylinder radiation resistance. (d) radiation resistance of a half cylinder radiating into a half space.

The differences between parts (a)-(d) of Fig. 4-7 are instructive. It can be seen right away that the full cylinder (Fig. 4-7(a)) and half cylinder (Fig. 4-7(b)) modes match BEM the best, with less than 2 dB of difference almost everywhere in the range. Half cylinder modes seem to give better performance in the small a region, especially at $a = 9.7$ cm, where the plate has been curved to a finite-length half cylinder. The average ΔL_{Π} is -1.1 dB for full cylinder modes and -0.8 dB for half cylinder modes. For large radii of curvature the flat plate and curved plate modes are just as accurate. We see that there is little advantage to the curved plate modes over the flat plate modes in many regions. At low a, high f and in some regions below 600 Hz the curved plate formulation gives a slight improvement over the flat plates, but elsewhere the improvement is negligible. The average ΔL_{Π} for these mode types is -1.7 dB for flat plates and -1.2 dB for curved plates.

In the comparison of these formulations it is important to know other reasons why certain modes may or may not be desirable. One is computational complexity; in calculating the radiation resistance, the curved modes take approximately an order of magnitude longer than the flat plate radiation resistance, and the eigenfunction expansion R takes an order of magnitude longer than that.

4.5 Conclusions

Several formulations for radiation modes of cylindrically curved plates have been presented, including a high-frequency diffraction-based formulation which has not been seen in the literature previously. These diffraction-based modes are seen to converge to the flat plate modes as the radius of curvature goes to infinity. The curved plate modes were explored in relation to the cylinder eigenfunction expansion modes and were found to match well at low curvatures.

Curved plate modes, cylindrical eigenfunction-based modes, both with and without a half-space baffle, and flat plate modes mapped to a curved surface were used to model sound radiation from a curved plate with endcaps backed by an infinite baffle. Though none of the modes presented were formulated for this scenario exactly, all of them were able to predict the sound power within 6 dB, and the cylinder modes were able to predict sound power within 2 dB in almost all of the curvature-frequency combinations tested. We see that modes match in scenarios that best fit the geometries they were designed for.

Chapter 5

Conclusions

5.1 Summary

After a brief review of the concept of radiation resistance matrices and their uses, a derivation of the eigenfunction expansion cylindrical radiation resistance matrix was presented. This produced a full, analytical expression for the matrix, which can be used in sound power calculations. The radiation modes computed from this matrix were shown to match multipole trends at low frequencies as would be expected from canonical radiation modes for other geometries. Numerical methods to evaluate the non-closed form equations were presented.

Following the derivation of the cylindrical radiation modes, sound power was computed for analytical simply-supported shell velocities using the VBRM method with these cylindrical modes. This power was compared to that calculated by BEM, which is treated as a benchmark. These results showed very good agreement between 0 Hz and 4 kHz with slight discrepancies of less than 1.5 dB appearing in some higher bands.

Experimental surface velocity measurements were collected using a SLDV and the sound power was determined using the VBRM method and the cylindrical radiation modes. The sound power was also measured using ISO 3741. These experimental results showed good agreement through the 10 kHz one-third-octave band. Between the 200 Hz and 10 kHz one-third octave bands the mean difference in the sound power obtained using ISO 3741 and the VBRM method was 0.1 dB with a standard deviation of 1.4 dB. The maximum difference between the two methods in any one-third octave band was 2.5 dB which occurred at the 400 Hz one-third octave band.

The results of the numerical simulations and the experimental work presented in Chapter 2 have shown that the cylindrical radiation resistance matrix and the accompanying acoustic radiation modes developed therein, implemented into the VBRM method, are useful tools which allow for the sound power measurement of cylinders. In addition, we see that modes developed for cylinders with infinite cylindrical baffles are able to accurately compute power for finite unbaffled cylinders.

Investigation was also made into the trends of these modes with frequency. It was shown that the most efficient radiation modes have peak wavenumbers that tend to follow the radiation circle as it moves with frequency. This is true regardless of the circumferential wavenumber of the modes. Only k_z changes with frequency to follow the radiation circle in this case. Similar analysis for the other structures given in Fig. 3-1 show that this morphing effect occurs in the z dimension for all three mode types shown in the figure, but in the θ dimension only for the partial cylinders on an infinite cylindrical baffle. Comparison with other known radiation modes, such as those for flat baffled plates and those for spheres, suggests that this morphing of radiation modes with frequency occurs only in dimensions where the structure does not span the whole dimensional space. For example, a vibrating sphere covers the whole ϕ and θ dimensions, over which the

fluid-structure interface is defined, and consequently there is no variation of the radiation modes with frequency. In contrast, the radiation modes of flat plates morph with frequency in both dimensions over which they are defined; this is because the flat plate does not cover the full breadth of either of those dimensions.

In addition to the eigenfunction mode formulations, a high-frequency diffraction-based formulation was given. The diffraction-based modes, or curved plate modes, are seen to converge to the flat plate modes as the radius of curvature goes to infinity. The curved plate modes were explored in relation to the cylinder eigenfunction expansion modes and were found to match well at low curvatures.

Curved plate modes, cylindrical eigenfunction modes, both with and without a dividing baffle, and flat plate modes mapped to a curved surface were used to model sound radiation from a curved plate with endcaps backed by an infinite baffle. Though none of the modes presented were formulated for this scenario exactly, all of them were able to predict the sound power within 6 dB, and the cylinder modes were able to predict sound power within 2 dB in almost all of the curvature-frequency combinations tested. We see that modes match in scenarios that best fit the geometries they were designed for.

5.2 Recommendations

The recommended continuation of this work includes further experimental verification of the expressions developed herein as well as extension of these expressions to more general geometries.

It is necessary still to verify the curved plate and partial cylinder expressions using experimental sound power measurements. The computational results of Chapter 4 could be recreated experimentally to this end. An adjustable plate which can be curved to various radii of

curvature has been fabricated and could be tested with an SLDV for this verification. In addition, the partial cylinder radiation resistance matrix given in Eqs. (3-7) and (4-7) could be verified experimentally by constructing a quarter cylinder that could use a two-wall corner of a room as an approximate baffle.

Of particular interest in further development of this work is the extension of the diffraction-based formulations to additional geometries. In addition to cylindrically curved objects, the work on the uniform theory of diffraction in electromagnetic radiation treated spherically curved surfaces as well as arbitrarily curved convex surfaces.[22] These expressions could be adapted for use in radiation modes to provide a very general alternative to boundary element methods for convex surfaces. Use of the scanning laser doppler vibrometer could then potentially serve a dual purpose of measuring the vibration of the surface and the curvature or shape of the surface. Combination of this diffraction-based ray theory with classical geometrical acoustics could allow for the treatment of surfaces that are not convex in a complete ray-based theory particularly well suited to the radiation mode problem.

REFERENCES

[1] G. V. Borgiotti, “The power radiated by a vibrating body in an acoustic fluid and its determination from boundary measurements,” *J. Acoust. Soc. Am.* **88**(4), 1884-1893 (1990).

[2] Y. Cao, S. D. Sommerfeldt, W. Johnson, J. D. Blotter, P. Aslani, “An analysis of control using the weighted sum of spatial gradients in active structural acoustic control for flat panels,” *J. Acoust. Soc. Am.* **138**(5), 2986-2997 (2015).

[3] M.R. Bai, M. Tsao, “Estimation of sound power of baffled planar sources using radiation matrices,” *J. Acoust. Soc. Am* **112**, 876-883 (2002).

[4] D. Fritze, S. Marburg, H.-J. Hardtke, “Estimation of radiated sound power: A case study on common approximation methods,” *Acta Acust. United Ac.* **95**, 833-842 (2009).

[5] S. J. Elliot and M. E. Johnson, “Radiation modes and the active control of sound power,” *J. Acoust. Soc. Am.* **94**(4) 2194-2204 (1993).

[6] D. M. Photiadis, “The relationship of singular value decomposition to wave-vector filtering in sound radiation problems,” *J. Acoust. Soc. Am.* **88**(2) 1152-1159 (1990).

[7] F. Fahy and P. Gardonio, “Sound radiation by vibrating structures,” *Sound and structural vibration, radiation, transmission and response, 2nd ed*., Academic Press, Oxford, UK, (2007).

[8] C. Jones, “Sound Power Calculations using a Scanning Laser Doppler Vibrometer and the Radiation Resistance Matrix,” M.S. Thesis, Brigham Young University (2019).

[9] Y. Cao, S. D. Sommerfeldt, W. Johnson, J.D. Blotter, P. Aslani, “An analysis of control using the weighted sum of spatial gradients in active structural acoustic control for flat panels” *J. Acoust. Soc. Am.* **138** 2986-2997 (2015).

[10] P. Aslani, S. D. Sommerfeldt, J. D. Blotter, “Active control of simply supported cylindrical shells using the weighted sum of spatial gradients control metric,” *J. Acoust. Soc. Am.* **143**(1), 271-280 (2018).

[11] D.R. Hendricks, W.R. Johnson, S.D. Sommerfeldt, and J.D. Blotter, “Experimental active structural acoustic control of simply supported plates using a weighted sum of spatial gradients” *J. Acoust. Soc. Am.* **136**, 2598-2608 (2014).

[12] J. Liu, Y. Liu, and J. S. Bolton, "The application of acoustic radiation modes to engine oil pan design," SAE Technical Paper 2017-01-1844 (2017).

[13] J. Liu, Y. Liu, and J. S. Bolton, “Acoustic source reconstruction and visualization based on acoustic radiation modes,” *J. Sound Vib.* **437** 358-372 (2018).

[14] A. Sarkissian, “Acoustic radiation from finite structures,” *J. Acoust. Soc. Am.* **90**(1), 574-578 (1991).

[15] G. V. Borgiotti and K. E. Jones, “Frequency independence property of radiation spatial filters,” *J. Acoust. Soc. Am.* **96**(6) 3516-3524 (1994).

[16] P. Aslani, S. D. Sommerfeldt, and J. D. Blotter, “Analysis of external radiation from circular cylindrical shells,” *J. Sound Vib.* **408** 154-167 (2017).

[17] J. Demmel, I. Dumitriu, and O. Holtz, "Fast linear algebra is stable," *Numerische Mathematik* **108**(1) 59-91 (2007).

[18] S. Winograd, “On the number of multiplications necessary to compute certain functions,” *Communications on Pure and Applied Mathematics* **23**(2) 165–179 (1970).

[19] J. Liu, Y. Liu, and J. S. Bolton, “A study of the frequency and shape dependency of acoustic radiation modes,” *Proc. InterNoise 2018,* Paper 1769 (2018).

[20] D. A. McNamara, J. A. G. Malherbe, and C. W. Pistorius. *Introduction to the uniform geometrical theory of diffraction*. Artech House, 1990.

[21] B. R. Levy and B. J. Keller, “Diffraction by a smooth object,” *Comm. Pur. Appl. Math.* **12**(1), 159-209 (1959).

[22] P. H. Pathak and N. Wang, “Ray analysis of mutual coupling between antennas on a convex surface,” IEEE Trans. Ant. Prop. **29**(6), 911-922 (1981).

[23] T. A. Pitts, R. H. Selfridge, D. M. Bhabries, “Solution of the Euler field equations for plane-wave scattering by an end-capped cylinder via the uniform geometrical theory of diffraction,” *J. Acoust. Soc. Am.* **94**(6), 3437-3447 (1993).

[24] P. H. Pathak and N. N. Wang, “An analysis of the mutual coupling between antennas on a smooth convex surface,” Report No. ESI-784583-7. Ohio State Univ. Columbus Electroscience Lab (1978).